An Apparatus for the Observation of Trapped Cd$^+$ Ion Interactions with Intense Laser Pulses

by

Russell Lowell Miller

A senior honors thesis submitted to

the Department of Physics of

the University of Michigan

College of Literature, Science and the Arts

in fullfilment of the course requirements for Physics 499

in submission for the 2003 W.L. Williams Award

and for the degree of

Honors B.S. in Physics

2003

This thesis entitled:
An Apparatus for the Observation of Trapped Cd$^+$ Ion Interactions with Intense Laser
Pulses
written by R.L. Miller
has been approved for submittal by

_____

Prof. Christopher Monroe

Date _____

_____

Russell L. Miller

Date _____

The final copy of this thesis has been examined by the research advisor and has been
found suitable for completion of the course requirements of Physics 499.

Abstract

Trapped Cd^+ ions offer a promising prospective system for implementation of fast quantum logic gates [1]. We relate the first work towards experimental realization of a new, highly scalable scheme for ion trap-based quantum computation [2]. For data bus, this "pushing gate" relies upon the entanglement of qubit ions in adjacent microtraps through the use of strong, off-resonant laser pulses. The magnitude of the a.c. Stark shift (and, implicitly, the dipole force) induced by these laser pulses depends upon the spin state of the qubit, producing potentially interesting spatial superpositions of the wavefunction associated with the ion.

We propose to apply a large a.c. Stark shift to a single Cd^+ ion located in a large, asymmetric RF quadrupole trap as a first step towards implementing the "pushing gate." The source of the "pushing" laser pulses is a frequency-quadrupled QuantaRay DCR-2 Q-switched Nd:YAG laser (outputting maximum 60mJ, $\sim$ 6ns pulses at 266nm with a repetition rate of 10Hz). These high intensity pulses, far red-detuned from both the Cd^+ D1 ($S_{1/2} \rightarrow P_{1/2}$, $\Delta_{12} \approx 197$ THz) and D2 ($S_{1/2} \rightarrow P_{3/2}$, $\Delta_{32} \approx 270$ THz) lines, will introduce a large a.c. Stark shift on the atomic ground state and, through interaction with the optical potential associated with the pulse, potentially impose a strong force on the ion. We outline the theory underlying the scheme as well as the construction of an experimental apparatus suitable for introducing strong pulses to the Cd^+ atomic system. Methods for observing and measuring this shift and future applications and directions are also discussed.

Acknowledgements

"The manifestation of a phenomenon is not detached from the observer - it is caught up and entangled in his individuality."

Johann Wolfgang von Goethe

First and foremost, thanks go out to all of the members of Professor Chris Monroe's trapped ion quantum information group (and especially to Prof. Monroe, for his seemingly boundless insight into every aspect of this research and for providing me this amazing opportunity). Tremendous thanks, in particular, are due to David Moehring, my coworker in designing, building and running this experiment. Without Dave, none of this could have come together as it did. Thanks also to Boris Blinov, Louis Deslauriers, and Martin Madsen for their invaluable advice and discussions on both the technical and theoretical aspects of this experiment.

On a personal note, I'd like to thank M. Giromini, my best buddy here at U-M, R. Bloomer, the "good" roommate, the entire 2001-2002 SPS crew, and the entire Ion Trappers broomball squad (who I've already thanked once above). Lastly, huge thanks to my parents for their support, kindness, and keen editorial sense.

Contents

Chapter

Tables

Table

Figures

Figure

Chapter 1

Introduction

Ion traps, in one form or another, have been workhorses in experimental physics for over 60 years now [3]. Laser cooling, now ubiquitous in almost every atomic physics experiment, was first observed in an ion trap in 1978 [4, 5]. Measurements of electron and positron g-factors taken in ion traps have provided some of the most precise tests of QED currently available [6]. Recent success with trapped $^{199}Hg^+$ ions [7] as a precision frequency standard may even herald the next generation of atomic clocks.

One of the most active areas of trapped ion research in recent years has been the application of trapped ions to quantum information science and, specifically, to quantum computing. Trapped atomic ions which closely approximate ideal two- or three-level quantum systems (such as Be^+, Hg^+ and Cd^+) have shown promise as potential quantum bits ("qubits"). In 1995 the first scheme for ion trap quantum computing, due to J.I. Cirac and P. Zoller [8], was presented, as was the first experimental realization of an ion trap quantum logic gate built by researchers at the National Institute of Standards and Technology in Boulder, Colorado [9]. This scheme employs the individual internal electronic states of multiple ions stored within a single trap as a data register and the collective motional state of the ions as a data bus. This type of logic gate scheme is currently the principal focus of most research groups working in ion trap quantum computing, and has resulted in a number of recent advances towards a practical experimental realization [10, 1, 11, 12]

In 2000, a second entirely unique, scheme for ion trap quantum computation was presented by Cirac and Zoller [2, 13, 14]. Again, the electronic states of individual ions represent individual qubits, but in this scheme each ion is stored in its own "microtrap" and a travelling "head" trap is brought to the qubit which is to be read/written. In one interpretation, an intense, fast pulse of laser light is then used to entangle the ions in the adjacent traps and information is transferred in this way from qubit to qubit. This "pushing gate" offers potential advantages over the earlier Cirac and Zoller proposal in terms of speed and the need for preparative cooling of the qubit ions.

The subject of this thesis is the experimental implementation of such pulses on single trapped Cd^+ ions. This chapter will focus on classical ion trap dynamics that can be used to describe the general motional dynamics of a trapped ion as well as on the internal electronic structure of cadmium ions and how this structure is electromagnetically addressed with laser light. Section 1.4 will conclude the chapter with a discussion of the synthesis of these ideas into an efficient, theoretical means for quantum computation.

1.1   Dynamics of an Ion in an Ideal RF Quadrupole Trap

While there are a variety of means for electromagnetically confining charged particles [3], for purposes of quantum computation the RF quadrupole (or *Paul*) trap is the only choice. Underlying this preference are the number of particles reasonably confined (from one to a few hundred), the lengthy periods of time over which they may be stored, and the SHO-like quantum dynamics of strongly cooled trapped ions. Paul traps are used exclusively throughout the experiment described here, and this section will provide a working description of their dynamics as a primer for later analysis.

1.1.1   The Classical Dynamics and the Mathieu Equation

Paul traps can take a variety of forms [3, 16], though they share a common principle of operation. The electrode configuration depicted in Figure 1.1(a) is representative

of what is necessary to achieve confinement, and is a fair approximation to those fab-

ricated for this experiment. In this ideal case, each of the three conducting surfaces

are hyperboloids of revolution and therefore symmetric in rotation about the specified

z-axis. The central, closed electrode (from which a cross-section has been removed in

the figure) is commonly referred to as the "ring" and the two others as "endcaps."

With a potential V_0 offset by some static voltage U_0 and oscillating sinusoidally at RF

frequency Ω_T applied to the ring electrode and with the endcaps held at ground with

respect to the RF, the potential inside the trap is:

$$V(x, y, z, t) = (U_0 + V_0 \cos(\Omega_T t)) \left(\frac{x^2 + y^2 - 2z^2}{d_0^2} \right), \tag{1.1}$$

or, defining a radial coordinate in terms of the x- and y-basis:

$$V(x, y, z, t) = (U_0 + V_0 \cos(\Omega_T t)) \left(\frac{r^2 - 2z^2}{d_0^2} \right). \tag{1.2}$$
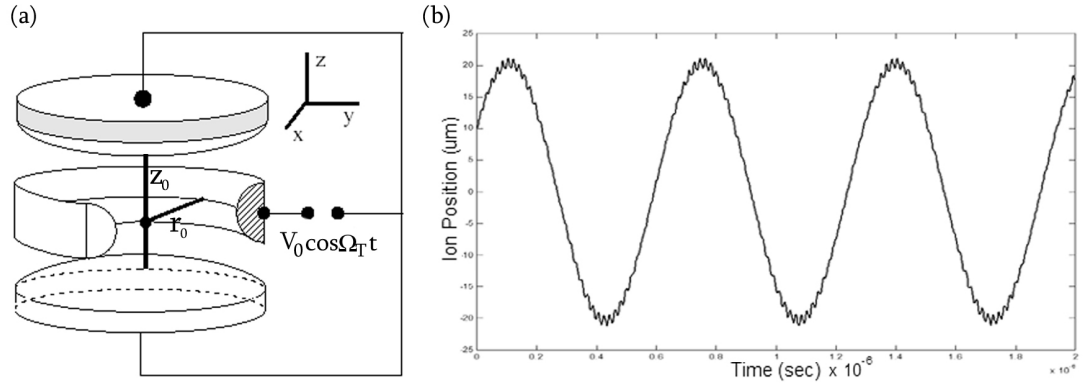
Figure 1.1: (a) The electrode configuration for an ideal Paul trap [15]. Each of the electrodes is a three-dimensional hyperboloid. An RF oscillating potential is applied to the ring electrode (from which a cross section has been removed) while the two endcaps are held at RF ground. (b) The one-dimensional motion of an ion trapped in a three-dimensional RF quadrupole trap of the type shown in (a). Note the overall sinusoidal oscillation ("secular motion") modulated at its extrema by the RF drive frequency Ω_T ("micromotion"). The trap parameters used to model this motion are approximately those of the real trap used for this work.

Here, d_0 is a characteristic geometric parameter of the trap, governed by the ring's innermost radius r_0 and the endcap-to-endcap spacing $2z_0$:

$$d_0 = \sqrt{r_0^2 + 2z_0^2}. \tag{1.3}$$

The motion of a point particle of mass m and charge Q placed within this potential is governed by a system of differential equations:

$$\frac{d^2r}{dt^2} + \left(\frac{2Q}{md_0^2}\right)(U_0 - V_0 \cos \Omega_T t)\, r = 0 \tag{1.4a}$$

$$\frac{d^2z}{dt^2} + \left(\frac{4Q}{md_0^2}\right)(U_0 - V_0 \cos \Omega_T t)\, z = 0 \tag{1.4b}$$

It is useful to perform the following change of variables on these equations:

$$a_r = -\frac{a_z}{2} = \frac{8QU_0}{md_0^2\Omega_T^2} \;;\; q_r = -\frac{q_z}{2} = \frac{4QV_0}{mr_2^2\Omega_T^2} \;;\; \zeta = \frac{\Omega_T t}{2} \tag{1.5}$$

Which yields:

$$\frac{d^2r}{d\zeta^2} + (a_r - 2q_r \cos 2\zeta)r = 0 \tag{1.6a}$$

$$\frac{d^2z}{d\zeta^2} + (a_z - 2q_z \cos 2\zeta)z = 0, \tag{1.6b}$$

where each of these equations has been expressed in the canonical form of the well-known Mathieu equation. It follows that when a_r, a_z, q_r and q_z each fall within the necessary range of values, solutions to (1.6a) and (1.6b) are bounded and, implicitly, the particle is trapped within the potential. Such solutions (the so-called Floquet solutions) take the form of an infinite series and are thus not very tractable for exploring the motion of the ion unless numeric techniques are employed [15]. Instead, a series of approximations to the problem offer considerably more practical insight.

1.1.2   The Secular Approximation

In order to represent clearly the dynamics of the particle, it is useful to approach the ion's motion along either the r- or z-directions as a sum of two components – a

small-amplitude, quickly oscillating term ("micromotion") and a large-amplitude, slowly oscillating term ("secular motion"). Consider, in z:

$$z \equiv z' + z_\mu \tag{1.7}$$

Returning to (1.4b) (with $U_0 = 0$):

$$\frac{d^2 z'}{dt^2} + \frac{d^2 z_\mu}{dt^2} = \left(\frac{4Q}{md_0^2}\right) V_0 \cos\left(\Omega_T t\right) \left(z' + z_\mu\right) \tag{1.8}$$

We assume $z' \gg z_\mu$ and $\ddot{z}_\mu \gg \ddot{z}'$, so

$$\frac{d^2 z_\mu}{dt^2} \approx \left(\frac{4Q}{md_0^2}\right) V_0 \cos\left(\Omega_T t\right) z' \tag{1.9}$$

Integrating this expression over a time t' sufficiently short that z' can be considered constant:

$$z_\mu(t) \approx -\left(\frac{4Q}{md_0^2 \Omega_T^2}\right) V_0 \cos\left(\Omega_T t\right) z' \tag{1.10}$$

In words, the micromotion of the ion is an oscillation at the RF drive frequency with an amplitude that is linear in the instantaneous magnitude of the secular motion.

We are left to determine the functional form of the secular motion, which is done by substituting (1.10) into (1.7):

$$z \approx z' - \left(\frac{4Q}{md_0^2 \Omega_T^2}\right) V_0 \cos\left(\Omega_T t\right) z' \tag{1.11}$$

Returning to (1.4b):

$$\frac{d^2 z}{dt^2} \approx \left(\frac{4Q}{md_0^2}\right) V_0 \cos\left(\Omega_T t\right) z' - \left(\frac{16Q^2}{m^2 d_0^4 \Omega_T^2}\right) V_0^2 \cos^2\left(\Omega_T t\right) z' \tag{1.12}$$

Since we have seen that the micromotion oscillates with frequency Ω_T, averaging (1.12) over a single RF period returns $\left\langle d^2 z_\mu / dt^2 \right\rangle = 0$ and we have:

$$\frac{1}{\pi} \int_0^\pi \frac{d^2 z}{dt^2} dt = \left\langle \frac{d^2 z'}{dt^2} \right\rangle$$
$$= -\frac{8Q^2 V_0^2}{m^2 d_0^4 \Omega_T^2} z' \tag{1.13}$$

It follows that on time scales larger than the period of the RF drive, the secular motion of the ion is approximated by the equation of motion for a simple harmonic oscillator with frequency of oscillation, ω_z:

$$\omega_z \approx \frac{2\sqrt{2}QV_0}{md_0^2\Omega_T} \tag{1.14}$$

Solving and substituting back into (1.7) along with (1.10), the total motion of the ion is given by:

$$z(t) \approx \cos(\omega_z t)\left(1 - \left(\frac{4Q}{md_0^2\Omega_T^2}\right)V_0\cos\left(\Omega_T t\right)\right) \tag{1.15}$$

Based on these approximations, the motion of the ion along z is then expected to be a large oscillation with frequency ω_z modulated (mainly at the larger oscillation's extrema) by smaller micromotion at the RF drive frequency. Figure 1.1(b), a Runge-Kutta-Felberg numerical integration of (1.6b), exhibits precisely these functional characteristics, verifying equation (1.15).

This description of confined motion within a trap, particularly the functional representation of micromotion (z_μ), holds promise as a gross means for determining the magnitude of forces induced upon the ion. Furthermore, we have shown that the motion of a trapped ion is approximately that of a simple harmonic oscillator. When extrapolated to the quantum limit of the ion's motion, the system exhibits the characteristics of a three-dimensional quantum SHO [3, 15]. The motional states of the ion in this limit are given by the generalized *Fock* (or *number*) states $|n\rangle$ as described in a variety of introductory references [17, 18]. This quantum treatment is of critical importance to both the original Cirac and Zoller scheme and the "pushing gate" scheme, and it will be discussed below.

1.2 The Atomic Structure of Cd$^+$

Thus far we have considered only the motion of an ion in a quadrupole trap with no regard for the ion's internal degrees of freedom. Trapped, singly ionized atomic
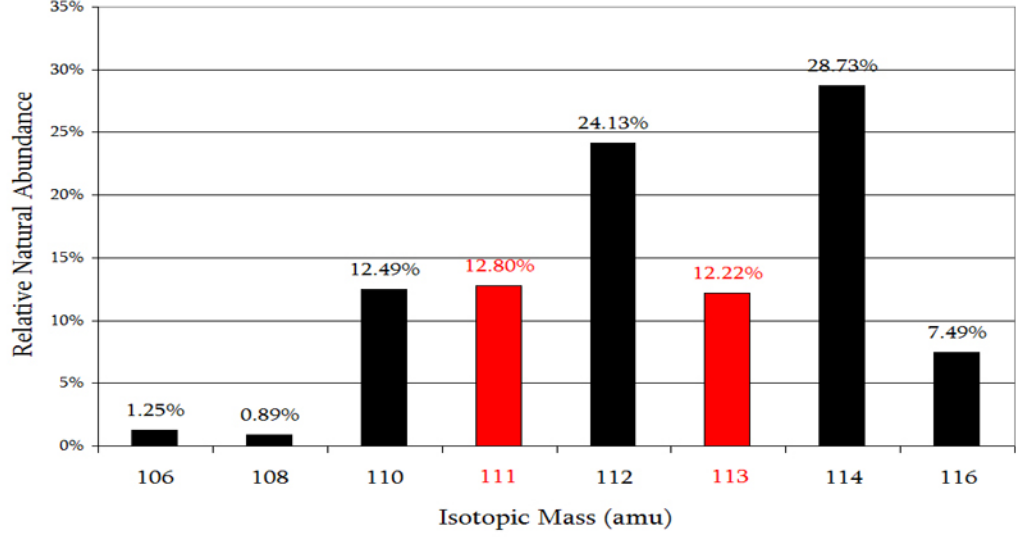
Figure 1.2: Diagram of the relative isotopic abundances of cadmium [19]. Isotopes shown in red are potential qubit ions with non-zero nuclear spin and associated hyperfine structure.

cadmium, which will be the medium for this experiment, offers a rich structure of electronic energy levels in each of the eight naturally stable isotopes (see Figure 1.2). Of particular importance among these isotopes are the two with odd atomic mass (^{111}Cd$^+$ and ^{113}Cd$^+$) and associated non-zero nuclear spin ($I = 1/2$ for both). Coupling of this spin to the spin of the ion's valence electron introduces hyperfine splitting of the ion's electronic energy levels. This experiment is mediated through the interaction of these hyperfine energy states with intense, monochromatic electromagnetic radiation (*ie:* laser light). Figure 1.3 shows the energy level structure for ^{111,113}Cd$^+$ in the $|F, m_F\rangle$ basis (shown also are the hyperfine qubit states $|1\rangle$ and $|0\rangle$ and the detuning of quadrupled Nd:YAG radiation the from $P_{1/2}$ and $P_{3/2}$ states). Appendix A depicts the same energy level structure along with the dipole matrix elements for each possible transition between states.

A "good" qubit manifests itself as a robust, two-level quantum system which can be addressed and prepared in a relatively accessible fashion. Any such system

$|e\rangle$ $\updownarrow$ ~800 MHz

D2: $S_{1/2} \leftrightarrow P_{3/2}$
~214.5nm

$\Delta_{32} \approx 270$ THz

$\updownarrow$ ~2.4 GHz

$\Delta_{12} \approx 197$ THz

Nd:YAG x 4
266nm

D1: $S_{1/2} \leftrightarrow P_{1/2}$
~226.5nm

σ^+

$|0\rangle$

0,0

$|1\rangle$

14.5 GHz – ^{111}Cd$^+$
15.4 GHz – ^{113}Cd$^+$

1,-1   1,0   1,1
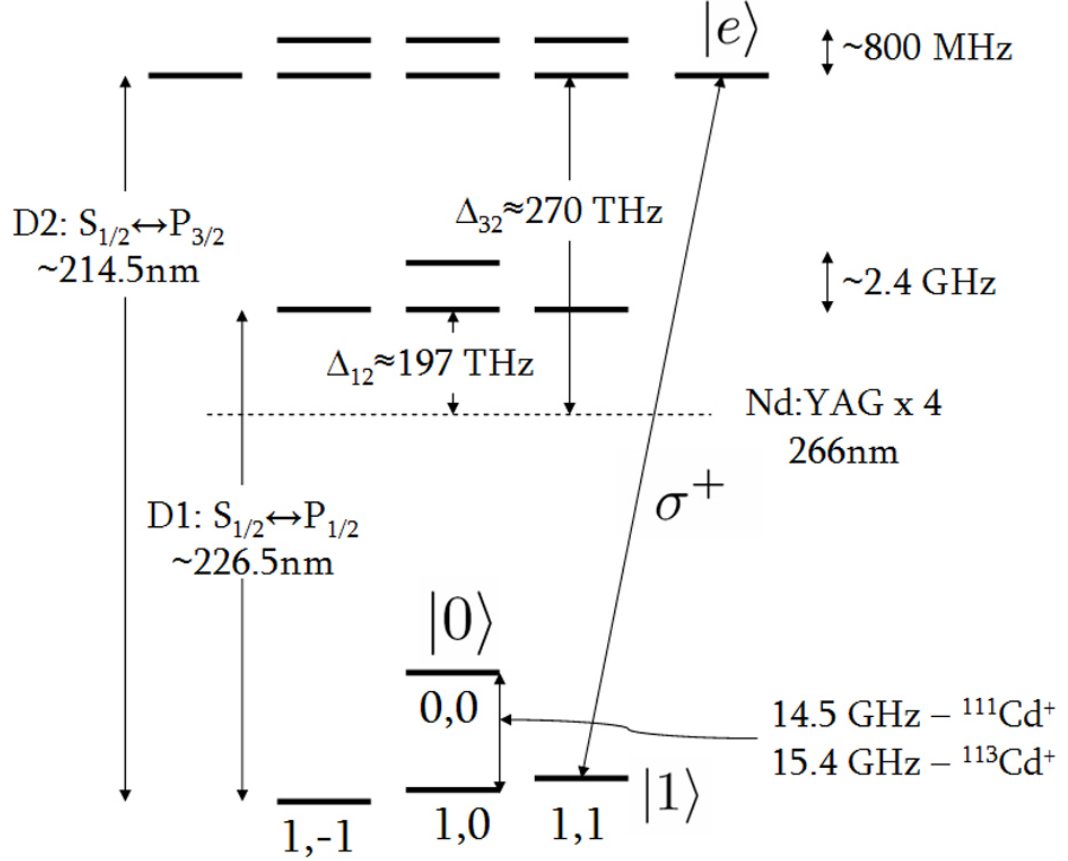
Figure 1.3: Representative (not to scale) energy level diagram for ^{113,111}Cd$^+$ in the $|F, m_F\rangle$ eigenbasis. The resonant wavelengths for the D1 ($^2S_{1/2} \leftrightarrow ^2P_{1/2}, \gamma_{1/2} \approx 37$MHz) and D2 ($^2S_{1/2} \leftrightarrow ^2P_{3/2}, \gamma_{3/2} \approx 47$MHz) transitions as well as the magnitude of the hyperfine splitting in each of the fine structure levels are pictured. Also represented is the resonant cycling transition (dipole matrix element of 1, see Figure A.2) between the $^2S_{1/2} |1, 1\rangle$ and $^2P_{3/2} |1, 2\rangle$, which is driven by a σ^+ polarized 214.5nm beam and used for detection of the ion. For reference in future sections, the detuning of light produced by frequency-quadrupling the Nd:YAG $^4F_{3/2} \rightarrow ^4I_{11/2}$ transition (266nm) from the $^2P_{1/2}$ (Δ_{12}) and $^2P_{3/2}$ (Δ_{32}) states is also shown.

is mathematically equivalent to a quantum spin, and this analogy will be employed throughout this discussion. As mentioned, the hyperfine structure of Cd^+ is what makes it so appealing, both as a qubit and as a candidate for implementing strong, spin-dependent forces. In particular, the $S_{1/2}$ manifold is used as a ground state with its two hyperfine levels corresponding to $F = 0, 1$ functioning as qubit levels; for this experiment, the $|0\rangle \equiv |0, 0\rangle$ state is effectively "spin down" while $|1\rangle \equiv |1, 1\rangle$ corresponds to "spin up." The Zeeman splitting between $|1, 0\rangle$ and $|1, -1\rangle, |1, 1\rangle$, in analogy to hydrogen, goes as the Bohr magneton:

$$\frac{\Delta\nu}{B} = \mu_B = 1.4\text{MHz}/\text{Gauss} \tag{1.16}$$

Within the trap, in its ground state, the ion is detected by optically pumping the system to the $|1\rangle$ state using a σ^+ (relative to the quantization axis of the ion) 214.5nm "detection" laser beam which is resonant with the $S_{1/2} \leftrightarrow P_{3/2}$ transition. Once pumped to $|1\rangle$, the detection beam drives a cycling transition (dipole matrix element of 1) between the ground state and the state labelled $|e\rangle$ in Figure 1.3. The 214.5nm light scattered by this transition is then used to resolve the state of the ion.

However, with the ion in the $|0\rangle$ state, the detection beam is ~ 15GHz detuned from $P_{3/2}$ and unable to couple to any transitions to other states. In order to make a transition from this "dark state" back to the $F = 1$ manifold, it is possible to add a 14.5GHz (15.4GHz for $^{113}Cd^+$) optical beatnote to the detection beam using an electro-optic modulator. Another recently cited method is to drive high-fidelity stimulated Raman transitions between the two states by again using an EO [20]. This technique involves Rabi oscillation between $|1\rangle$ and $|0\rangle$, allowing for the creation of coherent superpositions of qubit states.

Ultimately, the differences in how light couples to $|1\rangle$ and $|0\rangle$ will provide the spin-dependence of the laser-induced force which will be discussed in the next section. Just as with the detection beam, in the dark state the system will interact in a different

way with the detection laser than in the spin down state (by virtue of the detuning difference introduced by the hyperfine splitting). We will return to this concept in the final section of this chapter.

1.3   The a.c. Stark Shift and the Dipole Force

The last theoretical component to be considered is the nature of the laser-atom interaction which mediates the mapping of the Cd^+ spin state to the motion of the ion. Specifically, we will be addressing the a.c. Stark shift (or light shift) and the reactive dipole (or gradient) force on the associated ion. The simplest and most concise means for introducing both phenomena is to address each on a two-level atom and then extrapolate to the more complicated Cd^+ atomic structure. Alternate methods for performing the derivation below are given in references [21, 22].

1.3.1   The a.c. Stark Shift

Consider an electron in a simple atomic system consisting of two stationary eigenstates of the system Hamiltonian, $\mathcal{H}_0$, $|g\rangle$ (ground) and $|e\rangle$ (excited). We perturb the system with a laser field described by:

$$\vec{\mathcal{E}}(z,t) = E_0 \hat{\varepsilon} \cos(kz - \omega_\ell t) \tag{1.17}$$

We are interested in finding the motion of the system under this perturbation as governed by a new, interaction Hamiltonian, $\mathcal{H}'(t)$. In constructing this Hamiltonian, we make the key assumption that the two energy levels are coupled by electric dipole radiation from the laser in such a way that the spacial extent of the electron's wavefunction is orders of magnitude smaller than the optical wavelength λ of the laser. In this limit, we may ignore the spatial variation of $\vec{\mathcal{E}}(z,t)$ as we integrate over the Hamiltonian and thus we write (after some non-trivial algebraic manipulation [23]):

$$\mathcal{H}'(t) = -\hat{\mu} \cdot \vec{\mathcal{E}}(t). \tag{1.18}$$

Quantum mechanically, $\hat{\mu} \equiv e\hat{r}$, or, component-wise, $\mu_{jk} \equiv e \langle j|\hat{r}|k\rangle$ such that:

$$\mathcal{H}'_{jk}(t) = -\hbar \left(\frac{e \langle j|\hat{r}|k\rangle}{\hbar} E_0\right) \cos\left(\omega_\ell t\right)$$

$$= \hbar\Omega \cos(\omega_\ell t), \tag{1.19}$$

where we have defined the so-called Rabi frequency:

$$\Omega \equiv -\frac{e \langle e|\hat{r}|g\rangle}{\hbar} E_0. \tag{1.20}$$

An arbitrary, time-dependent wavefunction for an electron in this system takes the form:

$$|\psi(t)\rangle = c_e(t) |e\rangle e^{-\imath \omega_{eg} t} + c_g(t) |g\rangle e^{-\imath \omega_{ge} t}$$

$$= c_e(t) |e\rangle e^{-\imath \omega t} + c_g(t) |g\rangle e^{\imath \omega t}, \tag{1.21}$$

where we have noted that $\omega \equiv \omega_{eg} = -\omega_{ge}$.

The time evolution of this expression is described by the time-dependent Schrödinger equation as a coupled system of differential equations:

$$\imath\hbar\frac{dc_e(t)}{dt} = \frac{\hbar\Omega}{2}c_g(t)\left(e^{\imath(\omega+\omega_\ell)t} + e^{\imath(\omega-\omega_\ell)t}\right) \tag{1.22a}$$

$$\imath\hbar\frac{dc_g(t)}{dt} = \frac{\hbar\Omega^*}{2}c_e(t)\left(e^{-\imath(\omega+\omega_\ell)t} + e^{-\imath(\omega-\omega_\ell)t}\right). \tag{1.22b}$$

Assuming $|(\omega_\ell - \omega)| \ll \omega$, we invoke the rotating wave approximation (RWA), ignoring terms which oscillate quickly (at frequency $\omega_\ell + \omega$) with respect to those that oscillate slowly (at $\Delta \equiv \omega_\ell - \omega$) [23]:

$$\imath\hbar\frac{dc_e(t)}{dt} = \frac{\hbar\Omega}{2}c_g(t)e^{\imath\Delta t} \tag{1.23a}$$

$$\imath\hbar\frac{dc_g(t)}{dt} = \frac{\hbar\Omega^*}{2}c_e(t)e^{-\imath\Delta t}. \tag{1.23b}$$

We are principally concerned with determining the time-independent shift in energy of each of $|e\rangle$ and $|g\rangle$ induced by the laser, so we now move to a rotating frame in

which the weighting coefficients absorb the time dependence of $\mathcal{H}'(t)$. Redefining the c's:

$$c'_g(t) \equiv c_g(t) \tag{1.24a}$$

$$c'_e(t) \equiv c_e(t)e^{-\imath \Delta t}. \tag{1.24b}$$

Essentially, by requiring that the state vector precess at a frequency Δ, the Hamiltonian appears stationary. Substituting these new expressions into (1.23):

$$\imath \hbar \frac{dc'_e(t)}{dt} = \frac{\hbar \Omega}{2} c'_g(t) - \hbar \Delta c'_e(t) \tag{1.25a}$$

$$\imath \hbar \frac{dc'_g(t)}{dt} = \frac{\hbar \Omega^*}{2} c'_e(t). \tag{1.25b}$$

These expressions are entirely algebraically equivalent to (1.23). In matrix notation this new, static interaction Hamiltonian takes the form:

$$\mathcal{H}' = \frac{\hbar}{2} \begin{bmatrix} -2\Delta & \Omega \\ \Omega^* & 0 \end{bmatrix}. \tag{1.26}$$

The eigenvalues of this matrix are the energy shifts produced by the interaction:

$$E_{e,g} = -\frac{\hbar}{2}\left(\Delta \pm \sqrt{\Delta^2 + |\Omega|^2}\right). \tag{1.27}$$

It is reasonable under certain circumstances – when coupling these states with far-detuned radition of modest intensity – to assume $\Omega \ll |\Delta|$.[1]   In this approximation, Taylor expansion of the square root term in (1.27) leads to:

$$\Delta E_g = \frac{\hbar |\Omega|^2}{4\Delta} \tag{1.28a}$$

$$\Delta E_e = -\frac{\hbar |\Omega|^2}{4\Delta}. \tag{1.28b}$$

These perturbations are known, appropriately, as a.c. Stark shifts or light shifts. Qualitatively, it is worth noting that a red-detuned beam ($\Delta > 0$) shifts both $|g\rangle$ and $|e\rangle$ an equal amount apart whereas a blue-detuned beam ($\Delta < 0$) shifts the two closer. The

---

[1] The validity of this approximation in actual practice is discussed in the following chapter.

shift is also dependent on $\Omega^2 \sim E_0^2 \sim I_0$, the intensity of the beam. In this respect, a spatially-dependent optical intensity is equivalent to a spatially-dependent potential felt by the electron.

1.3.2 The Dipole Force and The Optical Potential

In the previous section, equation (1.28b) describes the shift in energy induced by an interaction with a laser for the ground state of a two-level atom as a function of laser detuning and Rabi frequency. While the detuning is a purely experimental quantity, the expression given in (1.20) for the Rabi frequency, however exact, does not relate Ω^2 to tangible experimental variables. In order to express the "dipole potential" (the potential felt by the electron because of the light shift as a function of the spatial characteristics of the laser beam) in purely experimental terms, we seek to re-define the square of the Rabi frequency.

In order to explore this problem, we introduce the density matrix formalism with regard to the two-level atom described in the previous subsection. In terms of the weighting coefficients c_e and c_g, above, the density matrix ρ is given as:

$$\rho \equiv \begin{pmatrix} \rho_{ee} & \rho_{eg} \\ \rho_{ge} & \rho_{gg} \end{pmatrix} = \begin{pmatrix} c_e c_e^* & c_e c_g^* \\ c_g c_e^* & c_g c_g^* \end{pmatrix}, \tag{1.29}$$

or, in terms of the rotating frame given by c_g' and c_e', above:

$$\tilde{\rho} = \begin{pmatrix} \rho_{ee} & \tilde{\rho}_{eg} \\ \tilde{\rho}_{ge} & \rho_{gg} \end{pmatrix} = \begin{pmatrix} c_e c_e^* & c_e c_g^* e^{-\imath \Delta t} \\ c_g c_e^* e^{\imath \Delta t} & c_g c_g^* \end{pmatrix}. \tag{1.30}$$

The terms $\tilde{\rho}_{eg}$ and $\tilde{\rho}_{ge}$ are known as coherences, while ρ_{gg} and ρ_{ee} describe the populations of the ground and excited states, respectively.

Any description of the evolution of the system in terms of the density matrix is entirely equivalent to the independent description given in the previous section. However, there is one aspect of the system which was not included in the previous discussion, but

proves crucial in "real" atoms: the spontaneous emission of light quanta of energy $\hbar\omega$ as the electron relaxes from the excited state to the ground state. The importance of this phenomenon and the technique for modeling it are discussed in a number of references [23]. Here, we simply assume it can be described as the decay of the coefficient $\rho_{eg}(t)$ at a rate $\gamma/2 = \omega^3\mu^2/6\pi\epsilon_0\hbar c^3$ (the linewidth), where μ is the dipole moment of the system:

$$\left(\frac{d\rho_{eg}}{dt}\right)_{S.E.} = -\frac{\gamma}{2}\rho_{eg}. \tag{1.31}$$

Using the analogues of equations (1.22) for the density matrix formalism, we arrive at what are known as the semiclassical optical Bloch equations (OBE):

$$\frac{d\rho_{gg}}{dt} = +\gamma\rho_{ee} + \frac{\imath}{2}\left(\Omega^*\tilde{\rho}_{eg} - \Omega\tilde{\rho}_{ge}\right) \tag{1.32a}$$

$$\frac{d\rho_{gg}}{dt} = -\gamma\rho_{ee} + \frac{\imath}{2}\left(\Omega\tilde{\rho}_{ge} - \Omega^*\tilde{\rho}_{eg}\right) \tag{1.32b}$$

$$\frac{d\tilde{\rho}_{ge}}{dt} = -\left(\frac{\gamma}{2} + \imath\Delta\right)\tilde{\rho}_{ge} + \frac{\imath}{2}\Omega^*\left(\rho_{ee} - \rho_{gg}\right) \tag{1.32c}$$

$$\frac{d\tilde{\rho}_{eg}}{dt} = -\left(\frac{\gamma}{2} - \imath\Delta\right)\tilde{\rho}_{eg} + \frac{\imath}{2}\Omega\left(\rho_{gg} - \rho_{ee}\right). \tag{1.32d}$$

In order to simplify this system of equations, we assume (with physical motivation) that the population of the system is conserved, $\rho_{gg} + \rho_{ee} = 1$, and that the optical coherences are related by $\tilde{\rho}_{eg} = \tilde{\rho}_{ge}^*$. Defining a new term, $w \equiv \rho_{gg} - \rho_{ee}$, the OBE can be re-expressed as two differential equations:

$$\frac{d\tilde{\rho}_{eg}}{dt} = -\left(\frac{\gamma}{2} - \imath\Delta\right)\rho_{eg} + \frac{\imath w\Omega}{2} \tag{1.33a}$$

$$\frac{dw}{dt} = -\gamma w - \imath\left(\Omega\tilde{\rho}_{eg}^* - \Omega^*\tilde{\rho}_{eg}\right) + \gamma. \tag{1.33b}$$

We are interested in the steady state solutions to these equations – particularly those in which the laser field is uniform. In this case $\dot{w} = \dot{\tilde{\rho}}_{eg} = 0$, and we solve:

$$w = \frac{1}{\left(1 + \frac{|\Omega|^2}{2}\frac{1}{\gamma^2/4 + \Delta^2}\right)} \tag{1.34a}$$

$$\tilde{\rho}_{eg} = \frac{\imath\Omega}{2\left(\gamma/2 - \imath\Delta\right)\left(1 + \frac{|\Omega|^2}{2}\frac{1}{\gamma^2/4 + \Delta^2}\right)} \tag{1.34b}$$

Both expressions bear the term:

$$s \equiv \frac{|\Omega|^2}{2} \frac{1}{\gamma^2/4 + \Delta^2} = s_0 \frac{1}{1 + (2\Delta/\gamma)^2} \tag{1.35}$$

$$s_0 \equiv \frac{2|\Omega|^2}{\gamma^2}. \tag{1.36}$$

We have arrived at a new relationship which describes how the quantity $|\Omega|^2$ governs the population of the system. We know from previous discussion that $\Omega(z) \sim \mathcal{E}(z)$; and thus it follows that $|\Omega(z)|^2 \sim I(z)$, the intensity of the laser. Thus we write:

$$s_0 = \frac{2|\Omega(z)|^2}{\gamma^2} \equiv \frac{I(z)}{I_{sat}} \tag{1.37}$$

$$\Rightarrow \quad |\Omega(z)|^2 = \frac{\gamma^2}{2} \frac{I(z)}{I_{sat}} \tag{1.38}$$

Where I_{sat} is a dimensionless constant of proportionality which depends upon (1.20), and can expressed in terms of experimental quantities as $I_{sat} \equiv \pi hc\gamma/3\lambda^2$.

Returning, at last, to equation (1.28b), we define the potential felt by the system in state $|g\rangle$:

$$U_{dip}(z) = \Delta E_g(z)$$

$$= \frac{\hbar}{8} \frac{I(z)}{I_{sat}} \frac{\gamma^2}{\Delta} \tag{1.39}$$

Taking the gradient of this potential, we arrive at the goal of this discussion: an equation describing the dipole force imposed on a simple two-level atom by an off-resonant laser beam:

$$F_{dip} = -\nabla U_{dip} = -\frac{\hbar}{8} \frac{\nabla I(z)}{I_{sat}} \frac{\gamma^2}{\Delta} \tag{1.40}$$

1.3.3 Generalizing to the Far Off-Resonant Regime

In order to arrive at equation 1.40, the RWA – that the effect of the quickly rotating terms of order $\exp(\omega_\ell + \omega)$ is negligible with respect to the more slowly rotating terms of order $\exp(\omega_\ell - \omega)$ – was made in subsection 1.3.1. This is often a valid
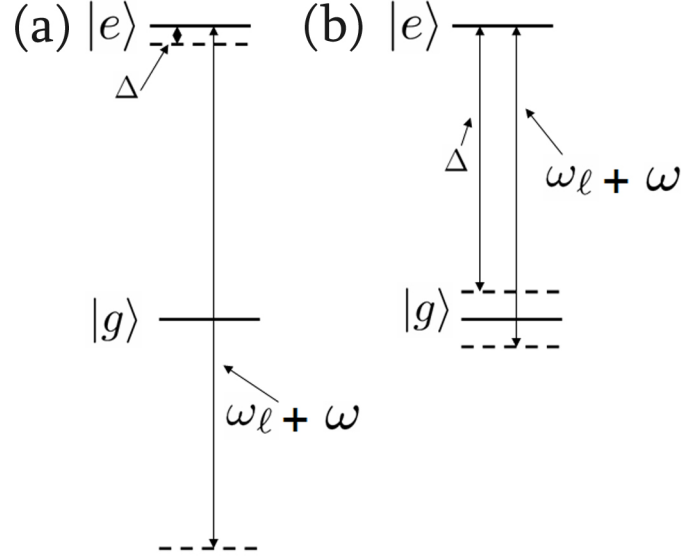
Figure 1.4: (a) Near-resonant radiation couples a two-level system. The counter-rotating frequency $(\omega_\ell + \omega)$ is far from the resonant transition, while the slowly rotating term $(\Delta = \omega_\ell + \omega)$ is very near. Here the RWA applies, and the contribution from counter-rotating is negligible. (b) In the case where Δ is on the order of $\omega_\ell + \omega$, both terms contribute significantly to the overall a.c. Stark shift.

approximation, especially when coupling the states of a pure two-level system with near-resonant radiation. However, in the case of a three-level system, light near resonance for one transition might couple weakly to a *far off-resonant* transition and induce a secondary a.c. Stark shift. In this far off-resonant regime, the RWA fails and we must approach the problem from a slightly different angle.

To visualize the problem, consider Figure 1.4. Generally, the RWA applies when $\Delta \ll \omega \ll (\omega_\ell + \omega)$, but fails when Δ is on the order of $(\omega_\ell + \omega)$. In this limit, equations (1.22) cannot be expressed in terms of a time-independent Hamiltonian matrixsuch as (1.26), and no closed form energy eigenvalues exist. However, in hydrogen-like systems such as Cd^+, it is often valid to regard the rotating and counter-rotating terms as individual beams coupled to the excited state with detunings of $\Delta \equiv \omega_\ell - \omega$ and $\Delta' \equiv \omega_\ell - \omega$, respectively [24]. Here Δ' is, equivalently, a second, counter-rotational detuning. By analogy, equation (1.28b), the magnitude of the a.c. Stark shift on the ground state

becomes:

$$\Delta E_g = -\frac{\hbar\Omega^2}{4}\left(\frac{1}{\Delta} + \frac{1}{\Delta'}\right).\tag{1.41}$$

Similarly, analogous to (1.39) and (1.40):

$$U_{dip}(z) = \frac{\hbar\gamma^2}{8}\frac{I(z)}{I_{sat}}\left(\frac{1}{\Delta} + \frac{1}{\Delta'}\right),\tag{1.42}$$

$$F_{dip}(z) = \frac{\hbar\gamma^2}{8}\frac{\nabla I(z)}{I_{sat}}\left(\frac{1}{\Delta} + \frac{1}{\Delta'}\right).\tag{1.43}$$

1.3.4   Application to the ^{111,113}Cd$^+$ System

The two-level system discussed above is, of course, an incomplete description of physical atoms comprised of many more than two electron energy levels coupled by dipole radiation. The principles and assumptions underlying the derivation of equation (1.40) are, nonetheless, applicable to these more complicated systems. Whereas for the two-level system the dipole transition strength is $\beta = 1$ for the single, allowed transition, in the multilevel case we generalize (1.38) to:

$$\Omega = \beta\frac{\gamma^2}{2}\frac{I}{I_{sat}}.\tag{1.44}$$

Or, in terms of the total dipole force on the atom for all m allowed transitions:

$$U_{dip} = \sum_m \beta_m \left(\frac{\hbar\gamma^2}{8}\frac{I(z)}{I_{sat}}\left(\frac{1}{\Delta} + \frac{1}{\Delta'}\right)\right)_m,\tag{1.45a}$$

$$F_{dip} = -\sum_m \beta_m \left(\frac{\hbar\gamma^2}{8}\frac{\nabla I(z)}{I_{sat}}\left(\frac{1}{\Delta} + \frac{1}{\Delta'}\right)\right)_m.\tag{1.45b}$$

The two equations given by (1.45) are directly applicable to the ^{111,113}Cd$^+$ system described in section 1.2. The dipole matrix elements which govern the coupling strengths β for each of the allowed transitions in Cd$^+$ are presented in Appendix A.

1.3.5   Spin-Dependent a.c. Stark Shifts

The structure of odd-isotope Cd$^+$ ions (Figure 1.3) is such that two qubit states in the $S_{1/2}$ manifold may experience a.c. Stark shifts of significantly different magnitudes

when addressed with light of a fixed polarization and detuning. This differential Stark shift is the result of a number of distinct effects – polarization selection rules, the structural differences between the $P_{1/2}$ and $P_{3/2}$ manifolds, hyperfine splitting in each of the fine structure levels, differences in the dipole matrix elements and linewidths for the D1 and D2 lines, and Zeeman splitting of the $F = 1$ submanifold of the $S_{1/2}$ state. The magnitude of each of these effects is governed by the detuning of the laser from resonance, the polarization of the beam, and the two $S_{1/2}$ hyperfine states being considered as spin (qubit) states.

With these parameters in mind, it is valuable to examine the following contrived but illustrative example. With $|0,0\rangle_{S12} \equiv |0\rangle$ and $|1,1\rangle_{S12} \equiv |1\rangle$ as the two qubit states, σ^+-polarized laser pulses of optical frequency ω_ℓ couple the system to the $P_{1/2}$ and $P_{3/2}$ manifolds. The a.c. Stark shift on $|1\rangle$ (which couples only to $P_{3/2}, F = 2, m_F = 2$) is given by (1.45b):

$$U_{|1\rangle}(z, \omega_\ell) = \frac{\hbar \gamma_{3/2}^2}{8} \frac{I(z)}{(I_{sat})_{3/2}} \left(\frac{1}{\omega_{3/2} - \omega_\ell} + \frac{1}{\omega_{3/2} + \omega_\ell} \right), \tag{1.46}$$

while the shift on $|0\rangle$ (which couples to $P_{3/2}, F = 1, m_F = 1$ and $P_{1/2}, F = 1, m_F = 1$) is:

$$U_{|0\rangle}(z, \omega_\ell) = \frac{\hbar}{24} I(z) \left(\frac{2\gamma_{3/2}^2}{(I_{sat})_{3/2}} \left(\frac{1}{\omega_{3/2} - \omega_\ell} + \frac{1}{\omega_{3/2} + \omega_\ell} \right) + \frac{\gamma_{1/2}^2}{(I_{sat})_{1/2}} \left(\frac{1}{\omega_{1/2} - \omega_\ell} + \frac{1}{\omega_{1/2} + \omega_\ell} \right) \right) \tag{1.47}$$

It is useful to find the zero of this equation (i.e., the laser frequency at which there is no net a.c. Stark shift upon the $|0\rangle$ level). Using given values for the linewidths and transition frequencies in question, we have:[2]

$$\omega_c = 8461 \text{THz} \quad \text{or,} \tag{1.48}$$

$$\lambda_c = 222.77 \text{nm} \tag{1.49}$$

It is worth noting that the counter-rotating terms in the expressions above (added as

---

[2] It is worth observing that this number is not entirely arbitrary – a laser of this wavelength could be
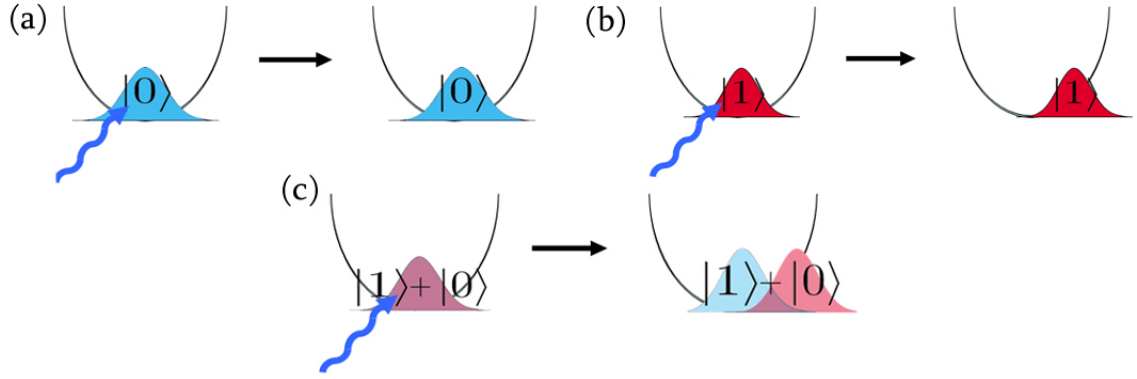
Figure 1.5: A representation of a spin-dependent force acting on a qubit in the pure states a.) $|1\rangle$ and b.) $|0\rangle$ as well as on the (unnormalized) superposition state c.) $\frac{1}{\sqrt{2}}(|1\rangle + |0\rangle)$. Note that the third case results in a mapping of the superposition of qubit spin onto a superposition of the ion's spatial wavefunction.

an extra measure for when the RWA fails) change the value of λ_c by only .03%.

A Cd$^+$ ion in the $|0\rangle$ state under these conditions will experience no net a.c. Stark shift, while an ion in the $|1\rangle$ state would experience some non-zero shift given by equation (1.46). An ion in the even superposition state $1/\sqrt{2}(|0\rangle + |1\rangle)$ will evolve into an a.c. Stark-shifted superposition. In this case, any dipole force resulting from interaction with the laser's optical potential will map the ion's internal electronic state onto its spatial wavefunction. This phenomenon is one practical realization of a spin-dependent force which will be crucial in the following discussion of the Cirac-Zoller "pushing gate" (see Figure 1.4 for an illustration of this principle).

1.4 A Microtrap-Based Scheme for Quantum Computation

1.4.1 The Original Theory

Finally, we describe the Cirac-Zoller "pushing gate" which motivates this entire discussion. It can be shown that any arbitrary quantum computational algorithm can be implemented through the use of a series of single qubit phase gates and two-qubit CNOT

realized experimentally by frequency quadrupling a Ti:Sapphire laser, or through use of a KrCl excimer laser.

gates [25]. A quantum system which can be manipulated to perform these operations with high fidelity is a potential quantum information processor.

Specifically, we define an operation $\mathbf{G}$ on a two qubit computational basis

$$\{|00\rangle, |01\rangle, |10\rangle, |11\rangle\} \tag{1.50}$$

as:

$$\mathbf{G} \equiv \sum_{\alpha,\beta=0}^{1} |\alpha\beta\rangle \langle\alpha\beta| e^{\Theta_{\alpha\beta}}, \tag{1.51}$$

equivalently:

$$\mathbf{G} = \begin{pmatrix} e^{\imath\Theta_{00}} & 0 & 0 & 0 \\ 0 & e^{\imath\Theta_{01}} & 0 & 0 \\ 0 & 0 & e^{\imath\Theta_{10}} & 0 \\ 0 & 0 & 0 & e^{\imath\Theta_{11}} \end{pmatrix}. \tag{1.52}$$

Through a series of unitary rotations, the operator $\mathbf{G}$ can be transformed into an operator P_ϑ, a general two-qubit phase gate (which applies a rotation only to the $|11\rangle$ state):

$$P_\vartheta = \begin{pmatrix} 0 & 0 & 0 & 0 \\ 0 & 0 & 0 & 0 \\ 0 & 0 & 0 & 0 \\ 0 & 0 & 0 & e^{\imath\vartheta} \end{pmatrix}. \tag{1.53}$$

where, neglecting a global phase of $(\Theta_{01} + \Theta_{10})/2$:

$$\vartheta = \Theta_{11} - \Theta_{10} - \Theta_{01} + \Theta_{00} \tag{1.54}$$

In the case $\vartheta = \pi$, the operator P_ϑ represents a two-qubit CNOT gate. Therefore, the evolution of any system represented by appropriate $\mathbf{G}$ can be transformed into a CNOT gate.

Now consider two ions, each in its own so-called "microtrap" – a miniature $(d_0 \sim 100\mu m)$ Paul trap of the type discussed in Section 1.2. These two traps are positioned so that there is an inter-ion spacing of $r \sim 1 - 500\mu$m, and a Coulomb repulsion is present between the ions. Both ions are prepared in the spin-dependent manner discussed for Cd^+ in subsection 1.3.4, with appropriate laser pulses of Gaussian profile and width τ interacting with them in an effectively simultaneous manner. We assume for now the adiabatic approximation that $\tau \gg (\omega_z)^{-1}$, where ω_z is the secular trap frequency – this approximation, used in the original Cirac-Zoller paper, is **not** valid in this experiment,however, and unnecessarily limits the gate speed. Under these conditions, $|0\rangle$ experiences no net Stark shift while $|1\rangle$ undergoes a net displacement $\bar{x}$ $(\bar{x} \ll r)$ because of the dipole force.

The Hamiltonian for this system is given by:

$$
\mathcal{H}_{\alpha,\beta} = \frac{p_\alpha^2}{2m} + \frac{\left(p_\beta'\right)^2}{2m} + \frac{1}{2}m\omega_z^2 \left(x_\alpha + r/2\right)^2 + \frac{1}{2}m\omega_z^2 \left(x_\beta' - r/2\right)^2
$$
$$
+ \left(v - x_\alpha - r/2\right) F_\alpha(t) + \left(v' - x_\beta' + r/2\right) F_\beta(t) + \frac{q^2}{4\pi\epsilon_0} \frac{1}{|x_\beta' - x_\alpha|} \qquad (1.55)
$$

where we have assumed a notation where primed coordinates correspond to the "second" ion, while unprimed coordinates correspond to the "first." Subscripts $\alpha = |1\rangle_1, |0\rangle_1$ and $\beta = |1\rangle_2, |0\rangle_2$ correspond to the internal states of the first and second ions respectively. The charge on each ion is given by q; and v and v' are a measure of the potential associated with the first and second Paul traps respectively when the ions are at equilibrium $(x_\alpha = r/2, x_\beta' = -r/2)$. The two quantities $F_\alpha(t)$ and $F_\beta(t)$ model the spin-dependent dipole force. It is beneficial [14] to move to a COM frame where the Hamiltonian can be re-written:

$$
\mathcal{H}_{\alpha,\beta} = \frac{p_\alpha^2}{2m} + \frac{\left(p_\beta'\right)^2}{2m} + \frac{1}{2}m\omega_z^2 \left[(x_\alpha - \bar{x}_\alpha)^2 - \bar{x}_\alpha^2 + 2\bar{x}_\alpha v\right]
$$
$$
+ \frac{1}{2}m\omega_z^2 \left[(x_\beta' - \bar{x}_\beta')^2 - (\bar{x}_\beta')^2 + 2\bar{x}_\beta' v'\right]
$$
$$
+ \frac{q^2}{4\pi\epsilon_0} \frac{1}{|r + x_\beta' - x_\alpha|}, \qquad (1.56)
$$

where we have:

$$\bar{x}_\alpha(t) = F_\alpha(t)/m\omega_z^2 \tag{1.57}$$

$$\bar{x}'_\beta(t) = F_\beta(t)/m\omega_z^2 \tag{1.58}$$

The evolution of this two-ion system is given by the unitary evolution operator [18]:

$$U_{\alpha,\beta} = \exp\left(-\frac{\imath}{\hbar}\int_{t_0}^t \mathcal{H}_{\alpha,\beta}(t')dt'\right), \tag{1.59}$$

as:

$$U_{\alpha,\beta}\left|\alpha\beta\right\rangle = e^{\imath\Theta_{\alpha,\beta}}\left|\alpha\beta\right\rangle. \tag{1.60}$$

In words, the dipole-force inducing pulse imposes a phase shift on the ions equal to:

$$\Theta_{\alpha,\beta} = -\frac{1}{\hbar}\int_{t_0}^t \mathcal{H}_{\alpha,\beta}(t')dt'. \tag{1.61}$$

Integrating (1.56) returns the sum of five independent terms. The first four of these are equivalent to single particle phases - unavoidable perturbations to the individual phase of each ion. However these are well known and can later be accounted for using single ion phase gates. The term of interest – the term containing the two-ion phase corresponding to ϑ, above – is the last term which results from the Coloumb interaction between the ions:

$$\phi_{\alpha,\beta} = -\frac{q^2}{4\pi\epsilon_0\hbar}\int_{t_0}^t \frac{1}{r + x'_\beta - x_\alpha}dt'. \tag{1.62}$$

Expanding this equation in a Taylor series about zero:

$$\phi_{\alpha,\beta} = -\frac{q^2}{4\pi\epsilon_0\hbar}\int_{t_0}^t \sum_{n=0}^\infty \left(\frac{x_\alpha - x'_\beta}{r}\right)^n dt'. \tag{1.63}$$

Examining this series, term-by-term we see that the zeroth order ($n = 0$) term contributes a uniform phase to both ions and thus can be neglected, the first order ($n = 1$) term contributes only linearly in x_α and x'_β and thus amounts to only single ion phases,

and, finally, the second order and higher ($n \geq 2$) terms contribute phase terms which apply to both ions and are thus the terms which are of concern for the logic gate operation.

1.4.2 Proposed Implementation

In their original paper [2], Cirac and Zoller proposed a system composed of a two-dimensional array of small traps as a quantum data register. Information is transferred to and from single ions stored in each trap by moving a single "head" trap from location to location and applying a pushing gate (see Figure 1.6) Information from any of the memory ions can be read onto the head ion, brought to another location and put through some quantum logic operation. Through repetition of this process an effective, constructed "quantum computer" has been constructed.
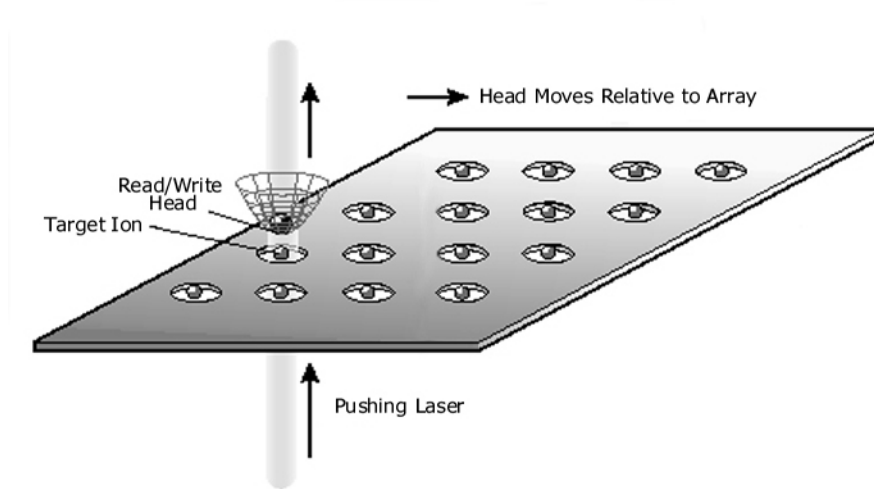

Figure 1.6: A two-dimensional array of microtraps for scalable quantum computation [2]. The head trap moves relative to the array, interacting with target ions through a strong dipole force induced by the interaction laser.

1.4.3   Limitations and the Fast Pulse Regime

In the theoretical discussion of the original pushing gate scheme the adiabatic approximation $\tau \gg (\omega_z)^{-1}$ was made. In general, practical ion traps are described by $\omega_z \approx 1\text{MHz}$, and so we are limited in the speed of the pushing gate by the restriction $\tau \gg 1\mu\text{s}$ or by a maximum gate repetition rate of a few hundred kilohertz. Ideally we would like to see much faster gate speeds and so we look to explore the regime wherein τ is very small.

In the original proposal, it is feasible to envision the ion "sloshing" slowly in the trap due to the pushing laser pulse and eventually returning, adiabatically, to its original state of motion as the pulse ends. Much shorter pulses can be regarded as an impulsive force on the ion, suddenly jarring the ion away from the center of the trap. Through constant repetition of such pulses, the ion could potentially gain a large amount of kinetic energy and become difficult to control in a coherent fashion. In order to counteract this effect it is possible to engineer the pushing pulses to bring the ion back to very nearly its initial position and momentum at the end of a pulse sequence. A paper describing this scheme and engineering the pulses necessary to implement it is currently under progress [26].

Chapter 2

Experimental Procedure

2.1   Experimental Parameters and Goals

The speed with which data is processed in a "pushing gate" is a function of the interaction time of the laser pulse with the trapped ion. We are limited in this parameter by the inverse of the natural linewidth γ for the off-resonant transition. In this limit, it is convenient to deal with nanosecond-scale laser pulses. Such pulses, if they are to impart an appreciable force upon the ions, must be of relatively high intensity and thus must induce large Rabi frequencies, Ω. Therefore we must address the state of the ions in the so-called *strong coupling regime* $(\Omega \gg \omega_z)$.

As a step toward the implementation of a "pushing gate," the goal of the research described in this thesis is the demonstration of spin-dependent a.c. Stark shifts and, potentially, dipole forces in the strong coupling regime of trapped Cd^+ ions. Specifically, this paper will outline the process of assembling the instrumentation and procedures necessary to observe and measure such effects. Because to rigid time constraints on the submission of this thesis, measurement data will not be available.

2.2   Inducing and Detecting the a.c. Stark Shift

2.2.1   Inducing the Shift

The ideal laser for inducing strong, differential, spin-dependent a.c. Stark shifts on the $|1,1\rangle$ and $|0,0\rangle$ states of a Cd^+ ion is a nanosecond pulsed laser at 222.71nm with a high repetition rate, single spatial mode, and little variation in energy from pulse to pulse. Such a laser is commercially available in the form of the Indigo DUV tunable, pulsed Ti:Sapphire laser from Positive Light Corp.. However, in order simply to demonstrate the principle underlying this phenomenon (and, perhaps, in the process, to demonstrate the need for the Indigo DUV laser), a significantly less costly pushing laser will be employed. This laser is the QuantaRay DCR-2 Q-switched, flashlamp-pumped Neodymium-Yttrium Aluminum Garnet (Nd:YAG) pulsed laser.

While details regarding the design and operation of this laser are presented in the next chapter, the parameters of this experiment must be specified with respect to the pushing laser, and so a few aspects of the DCR-2 are worth mentioning here. The DCR-2, Q-switched and fully amplified, produces ~ 800mJ, $8-9$ns-wide pulses with a rep-rate of 10Hz at the YAG fundamental 1064nm line. By passing this light through a properly phase-matched deuterated potassium dihydrogen phosphate (KD*P) crystal, the fundamental is converted into ~ 200mJ of 532nm light in $6-7$ns wide pulses. A second phase-matched KD*P crystal doubles the second harmonic to the YAG 4th harmonic at 266nm in ~ 60mJ, $4-5$ns pulses.

This light is 270THz detuned from the D2 line (at 214.5nm), and 197THz detuned from the D1 line (at 226.5nm) (see Figure 1.3). The energies per pulse given for each of the laser harmonics indicate the maximum value and are continuously variable to under 500μJ per pulse by adjusting the polarization of the fundamental injected into the first KD*P crystal. These pulses can be of sufficient intensity and detuning when focused to a narrow waist on the the ion to produce a large differential a.c. Stark shift between the

qubit states (though the shift on $|0\rangle$ will be nonzero). The magnitude of this induced differential shift will be discussed in the next subsection.

The DCR-2 has a few significant limitations. First is the 10Hz repetition rate of the laser's pulses. While logic operations can be performed on nanosecond time scales, the delay from operation to operation (and from individual experiment to experiment) is on the order of milliseconds. Also, because of inhomogeneity in the intensity of the flashlamp bursts which pump the laser, the pulse energy stability for the DCR-2 is only $\pm 4\%$. Lastly, because of the cavity design of the laser, both the spatial and temporal modes of the beam are very high order and non-Gaussian. These last two limitations make it difficult consistently to model the spatial intensity profile of the focused beam, $I(z)$, which is needed in equation (1.45) to determine the dipole force upon the ion.

2.2.2 Characterizing the Shift

We are able to characterize the energy per pulse by extracting a small sample of the pushing beam from a calibrated 95/5 fused silica beam splitter. The less intense beam is measured with an Ophir Optronics PE-25BB pyroelectric power sensor which returns per-pulse energy at 266nm with an error of $\pm 5\%$. Using this sensor, it is also possible to make a gross characterization of the laser's spatial mode in the far-field. By incrementally inserting a razor blade across the profile of the beam and measuring the average energy per pulse of the transmitted portion of the beam over a few hundred pulses, we were able to measure a rough cross-sectional intensity profile along horizontal and vertical axes (Figure 2.1). In general, this procedure was limited by fluctuations in the temporal mode of the beam and by limited resolution of the micrometer used to translate the razor and at best, provides confirmation that the beam is far from TEM_{00}. Given the non-Gaussian nature of the beam, it is useful to treat the intensity of the focused beam as a Heaviside step of height I_0 and width equal to the theoretical

"Gaussian" beam waist, w, where:

$$I_0 = \frac{4\pi E_{\text{pulse}}}{w^2}. \tag{2.1}$$

Here, E_{pulse} is a quantity measured with the pyroelectric sensor and w can be determined experimentally by measuring the transmission of the focused beam through incrementally smaller pinholes.

In this approximation, the dipole force cannot be treated because there is no spatial gradient of the beam's intensity at the ion. The a.c. Stark shift on the ground state is still present and is given by:

$$\Delta E_g = \sum_m \beta_m \left(\frac{\pi \hbar \gamma^2}{2w} \frac{E_{\text{pulse}}}{I_{sat}} \left(\frac{1}{\Delta} + \frac{1}{\Delta'} \right) \right)_m, \tag{2.2}$$

uniformly throughout the cross-sectional area of the beam. This formula resulted in Chapter 1 primarily from the approximation $\Omega \ll |\Delta|$. This condition is not guaranteed in the limits of large values of E_{pulse} and small values of w, though its functional form is much more tractable than the exact solution. Table 2.1 presents the approximate error in the magnitude of the a.c. Stark shift at 266nm due to this approximation (calculated for the shift on state $|1,1\rangle$ in σ^+ radiation).
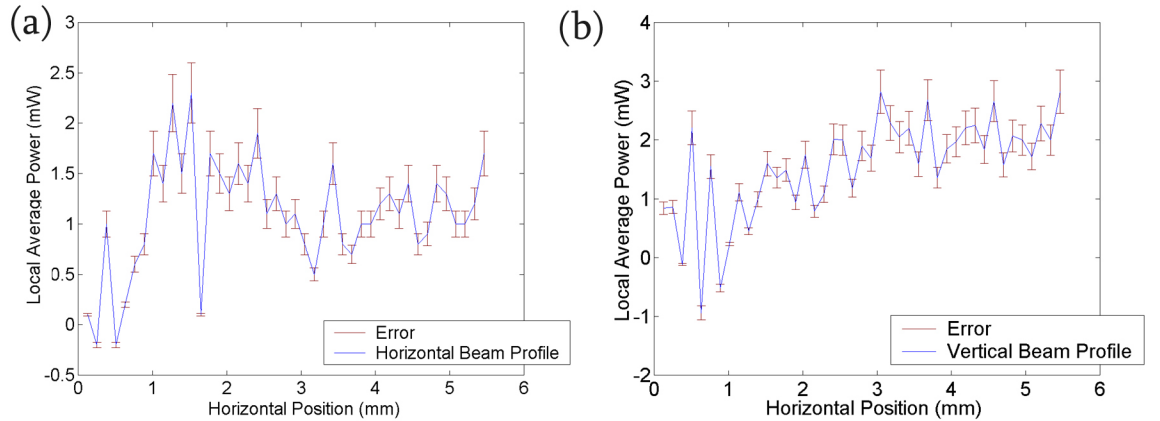

Figure 2.1: By incrementally moving a razor blade into the beam path of the DCR-2, the energy as a function of spatial location in the cross section of the beam (as a broad horizontal or vertical area) is mapped.

Table 2.1: Lookup table for error in a.c. Stark shift magnitude due to the approximation $\Omega \ll |\Delta|$. The horizontal lookup gives the pulse energy in mJ while the vertical lookup gives beam waist in μm. The error in equation (2.2) is given in percent as function of the two lookups.

	1mJ	3mJ	5mJ	7mJ	9mJ	11mJ	13mJ	15mJ	17mJ	19mJ	21mJ
5μm	0.68	2.02	3.32	4.59	5.83	7.05	8.24	9.40	10.55	11.67	12.77
10μm	0.17	0.51	0.85	1.19	1.52	1.85	2.18	2.51	2.83	3.16	3.48
15μm	0.08	0.23	0.38	0.53	0.68	0.83	0.98	1.13	1.28	1.43	1.58
20μm	0.04	0.13	0.21	0.30	0.38	0.47	0.55	0.64	0.72	0.81	0.89
25μm	0.03	0.08	0.14	0.19	0.25	0.30	0.36	0.41	0.46	0.52	0.57
30μm	0.02	0.06	0.10	0.13	0.17	0.21	0.25	0.28	0.32	0.36	0.40
35μm	0.01	0.04	0.07	0.10	0.13	0.15	0.18	0.21	0.24	0.27	0.29
40μm	0.01	0.03	0.05	0.07	0.10	0.12	0.14	0.16	0.18	0.20	0.22
45μm	0.01	0.03	0.04	0.06	0.08	0.09	0.11	0.13	0.14	0.16	0.18
50μm	0.01	0.02	0.03	0.05	0.06	0.08	0.09	0.10	0.12	0.13	0.14
55μm	0.01	0.02	0.03	0.04	0.05	0.06	0.07	0.08	0.10	0.11	0.12
60μm	0.00	0.01	0.02	0.03	0.04	0.05	0.06	0.07	0.08	0.09	0.10
65μm	0.00	0.01	0.02	0.03	0.04	0.04	0.05	0.06	0.07	0.08	0.09
70μm	0.00	0.01	0.02	0.02	0.03	0.04	0.05	0.05	0.06	0.07	0.07
75μm	0.00	0.01	0.02	0.02	0.03	0.03	0.04	0.05	0.05	0.06	0.06
80μm	0.00	0.01	0.01	0.02	0.02	0.03	0.03	0.04	0.05	0.05	0.06
85μm	0.00	0.01	0.01	0.02	0.02	0.03	0.03	0.04	0.04	0.05	0.05
90μm	0.00	0.01	0.01	0.01	0.02	0.02	0.03	0.03	0.04	0.04	0.04
95μm	0.00	0.01	0.01	0.01	0.02	0.02	0.02	0.03	0.03	0.04	0.04
100μm	0.00	0.01	0.01	0.01	0.02	0.02	0.02	0.03	0.03	0.03	0.04

It follows that for values of w greater than about 20μm and pulse energies less than 10mJ, the error due to the approximation is negligible. This, then, will be the regime in which the measurement of the a.c. Stark shift will be performed.

2.3   The Experiment

In order to measure the a.c. Stark shift, a single Cd^+ ion will be trapped and stored in an asymmetric quadrupole trap of the kind discussed in the first chapter and in more detail in the Chapter 3. The state of the ion will be prepared using cw lasers, and then a Ramsey experiment will be performed with the focused strong laser pulse inducing the phase shift which will be measured interferometrically.

2.3.1   Ramsey Interferometric Detection

2.3.1.1   Theory

The hyperfine qubit states in Cd^+ which are manipulated by the pushing beam can be viewed, as can all qubits, as a spin vector [25]. As such, as the evolution of the system between $|0\rangle$ and $|1\rangle$ can be modelled as rotation of the state vector about the Bloch sphere. The detection of pushing laser-induced a.c. Stark shifts will be treated in this respect as a canonical Ramsey experiment. A slight variation on this technique was recently reported for low-intensity laser beams on $^{40}Ca^+$ ions [27].

The experimental procedure begins by preparing the ion in the $|\Psi\rangle = |0\rangle$ state (by optically pumping there using an electrooptic modulator, for instance). Next a short "$\frac{\pi}{2}$"-pulse of 14.5GHz microwave radiation (resonant with the $|0\rangle \leftrightarrow |1\rangle$ transition) is applied. This rotates the spin vector in the Bloch sphere to the state

$$|\Psi\rangle = \frac{1}{\sqrt{2}}\left(|0\rangle + \imath |1\rangle\right). \tag{2.3}$$

A few microseconds after the $\frac{\pi}{2}$-pulse, the pushing laser is triggered to fire and is focused upon the ion. The system evolves according to the unitary evolution operator:

$$U = e^{-\frac{\imath}{\hbar} \int_0^\tau \mathcal{H}'(t)dt}, \tag{2.4a}$$

$$= e^{-\frac{\imath}{\hbar} \sum_\alpha \Delta E_\alpha \tau}, \tag{2.4b}$$

$$= e^{-\frac{\imath \pi \tau}{2w} \sum_\alpha \left(\sum_m \beta_m \left(\gamma^2 \frac{E_{\text{pulse}}}{I_{sat}} \left(\frac{1}{\Delta} + \frac{1}{\Delta'} \right) \right)_m \right)_\alpha}, \tag{2.4c}$$

where α sums over $|0\rangle$ and $|1\rangle$. Essentially, the strong pulses shifts the phase of the spin vector by an angle:

$$\phi_\alpha = \frac{\pi \tau}{2w} \sum_m \beta_m \left(\gamma^2 \frac{E_{\text{pulse}}}{I_{sat}} \left(\frac{1}{\Delta} + \frac{1}{\Delta'} \right) \right)_m, \tag{2.5}$$

so that after the pulse, the state vector of the ion is given by:

$$|\Psi\rangle = \frac{1}{\sqrt{2}} \left(e^{-\imath \phi_0} |0\rangle + \imath e^{-\imath \phi_1} |1\rangle \right) \tag{2.6a}$$

$$= \frac{e^{-\imath \phi_0}}{\sqrt{2}} \left(|0\rangle + \imath e^{-\imath \Delta \phi} |1\rangle \right) \tag{2.6b}$$

where $\Delta\phi$ is the differential phase shift between the two states.

Next, a second $\frac{\pi}{2}$-pulse is applied such that the strong pulse falls exactly in between it and the first. This rotates the state of the ion to:

$$|\Psi\rangle = \frac{e^{-\imath \phi_0}}{2} \left(\left(1 - e^{-\imath \Delta \phi} \right) |0\rangle + \imath \left(1 + e^{-\imath \Delta \phi} \right) |1\rangle \right) \tag{2.7}$$

In order to detect this state we measure fluorescence from the $|1\rangle \leftrightarrow |2, 2\rangle$ cycling transition, and so we project (2.7) onto $|1\rangle$:

$$P_1 = \langle 1|\Psi\rangle = \frac{\imath e^{-\imath \phi_0}}{2} \left(1 - e^{-\imath \Delta \phi} \right) \tag{2.8}$$

Ignoring the global phase:

$$P_1 = \frac{1}{2} \left(1 + \cos^2 \left(\Delta\phi \right) \right) \tag{2.9}$$

Therefore, by measuring ion fluorescence as a function energy per pulse from the DCR-2, a fringe pattern of frequency $\Delta\phi$ appears and can be used to determine the differential interaction of the pushing laser with the qubit states of a single ion.
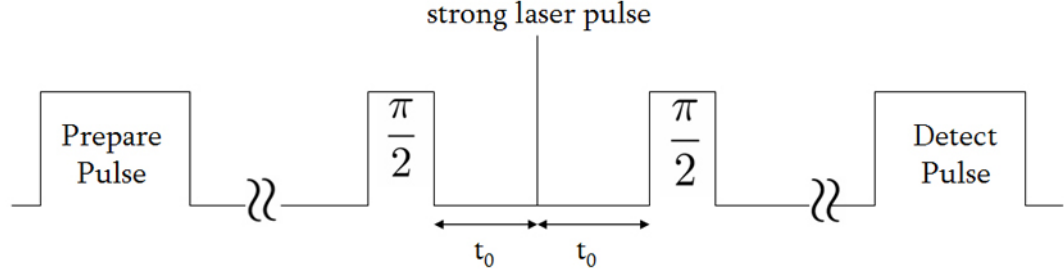
strong laser pulse

Figure 2.2: The sequence of pulses needed to carry out a phase detection Ramsey experiment. The prepare pulse at 214.5nm pumps the system to the $|0\rangle$ state, the $\frac{\pi}{2}$ pulse is a 14.5GHz microwave pulse which rotates the system's spin vector 90° in the Bloch sphere, the strong laser pulse at 266nm is as described above, followed by another $\frac{\pi}{2}$ pulse and finally a pulse which drives the $|1\rangle$ cycling transition (which scatters detectable light).

By solving equation (2.5) for a variety of values of E_{pulse} and w, a lookup table presenting induced differential phase shift in radians with pulse energy and beamwaist as indices is presented in Table 2.2.

2.3.1.2 Implementation

The series of pulses which comprise the method described above is illustrated in Figure 2.2. These pulses are implemented experimentally in LabView through a simple user interface which controls a Berkeley Nucleonics Corp. TTL pulse generator. The preparation and detection pulses are controlled using an acousto-optic modulator to switch the cw 214.5nm detection beam on or off. When preparing, an additional 6.8GHz "repumper" beatnote (in the blue) is added to the beam using an electro-optic modulator driven by a TTL switchable HP 8684D signal generator. The $\frac{\pi}{2}$ pulses are generated using an HP 8672A synthesized microwave generator operating at 14.5GHz which is externally switched by an American Microwave Corp. high-speed SPDT microwave switch. These microwave pulses are coupled into a custom-built KU-band directional

Table 2.2: A lookup table for a.c. Stark shift-induced differential phase shift (in radians) on the state vector of the ion. The horizontal lookup gives the pulse energy in mJ while the vertical lookup gives beam waist in μm. Calculations have assumed a uniform intensity distribution (as discussed above) and a 5ns strong pulse width.

	1mJ	**2**mJ	**3**mJ	**4**mJ	**5**mJ	**6**mJ	**7**mJ
5μm	563.377	1126.755	1690.132	2253.509	2816.886	3380.264	3943.641
10μm	140.844	281.689	422.533	563.377	704.222	845.066	985.910
15μm	62.597	125.195	187.792	250.390	312.987	375.585	438.182
20μm	35.211	70.422	105.633	140.844	176.055	211.266	246.478
25μm	22.535	45.070	67.605	90.140	112.675	135.211	157.746
30μm	15.649	31.299	46.948	62.597	78.247	93.896	109.546
35μm	11.497	22.995	34.492	45.990	57.487	68.985	80.482
40μm	8.803	17.606	26.408	35.211	44.014	52.817	61.619
45μm	6.955	13.911	20.866	27.821	34.776	41.732	48.687
50μm	5.634	11.268	16.901	22.535	28.169	33.803	39.436
55μm	4.656	9.312	13.968	18.624	23.280	27.936	32.592
60μm	3.912	7.825	11.737	15.649	19.562	23.474	27.386
65μm	3.334	6.667	10.001	13.334	16.668	20.002	23.335
70μm	2.874	5.749	8.623	11.497	14.372	17.246	20.121
75μm	2.504	5.008	7.512	10.016	12.519	15.023	17.527
80μm	2.201	4.401	6.602	8.803	11.003	13.204	15.405
85μm	1.949	3.899	5.848	7.798	9.747	11.696	13.646
90μm	1.739	3.478	5.216	6.955	8.694	10.433	12.172
95μm	1.561	3.121	4.682	6.242	7.803	9.364	10.924
100μm	1.408	2.817	4.225	5.634	7.042	8.451	9.859

microwave horn and inserted into the trap.

Ideally, we would set the pushing laser to a given energy per pulse, run the experiment some large number of times, average that set of data (i.e.: photon scatter rate as collected by the high quantum efficiency Hamamatsu PMT described in the next chapter), plot the data point, and move on to the next value of energy per pulse. However, as discussed, we are limited in our experiment by the significant fluctuations in energy per pulse from the DCR-2 pushing laser. For a given DCR-2 control setting, data will pour in for energy per pulses in a $\pm 4\%$ around a single value, which will effectively wash out the expected cosine squared dependency. In order to eliminate this problem, we propose a "back-office feed-forward" mechanism whereby for each data point a small portion of the pushing beam will be picked off using a calibrated beam splitter and measured to a few tenths of a percent accuracy using an Ophir Optronics 25BB-PE SmartHead. As the experiment runs, we simply feed the points into a database where they are sorted into bins corresponding to the energy of the pulse associated therewith. As this data is binned and plotted, we expect to see a cosine squared dependence, as derived above, which will confirm the strong field a.c. Stark interaction is as described. A National Instruments LabView program to automate this process is currently being designed and written.

2.3.2   Experimental Concerns

There are a few relative unknowns in this experiment as well. This is arguably the first experiment in which an ion is addressed in the so-called "strong excitation regime" [28] wherein the Rabi frequency is much larger than the trap secular frequency ($\Omega \gg \omega_z$). In fact, for a pushing beam producing 5mJ per pulse at a 30μm waist, the approximate Rabi frequency in the ion will be almost seven orders of magnitude larger than the trap frequency. A few concerns – particularly with regard to the high intensity of the pushing pulses – need to be addressed.

One of the challenges associated with using the DCR-2 is safely steering the tightly focused beam through the trap and out the other end of the chamber. We have observed that, at its focus, the beam is capable of ablating through a 125μm-thick sheet of molybdenum – the same material used to construct the trap – in around 10 pulses (or one second). Any incidence upon the trap could potentially destroy the electrodes and pollute the local vacuum. Additionally, the amount of 266nm light scattered during an interaction between the beam and the trap could potentially damage the sensitive positional PMT used to image fluorescence from the ion. The trap must be large enough so that if it is vibrating significantly, for any reason, the optical access through the trap is of sufficient area to pass the beam. Additionally, a filter which blocks 266nm and passes 214.5 is a desirable optic for the imaging apparatus. The optical viewports through which the beam passes into the vacuum chamber must be highly transmitting at 266nm in order to prevent backscatter and they must also be mechanically stable under thermal shock induced by beam as it is transmitted. These issues are addressed in the next chapter in a discussion of a discussion of the apparatus built specifically for this experiment.

One final concern is that the pushing laser may drive multiphoton second ionization of the Cd^+ target ion (producing trapped Cd^{2+} ions). The second ionization potential of cadmium is 16.9eV and 266nm photons carry 4.7eV of energy which means this would be a 4-photon interaction. Modeling multiphoton ionization theoretically in a complicated atomic system is a difficult matter. The best indication as to whether this will be a problem for the experiment is simply to apply the beam and observe the effect [29]. Experimental tests are pending.

Chapter 3

Experimental Apparatus

3.1   Design and Construction of a Paul Trap

3.1.1   The Vacuum Chamber

There were two principal criteria used to select the optimal trap vacuum chamber for this experiment. First, the stringent optical access requirements of the strong beam dictated that the beam should enter and leave the chamber at normal incidence through 266nm AR coated windows in order to minimize secondary reflections. The remaining detection (and potentially Raman) cw beams required a 45º geometry and so a Madgeburg spherical, cubical, or octagonal chamber could have proven feasible. The second requirement was that the trapping region be located within $\sim$ 10mm of an optical viewport in order to obtain the proper objective distance for the imaging PMT. This narrowed the possibilities down to a thin spherical octagon (see Figure 3.1).

The resulting chamber offers eight $1\frac{1}{3}$" Conflat (CF) feedthrough ports on its side and two $4\frac{1}{2}$" CF feedthroughs on top and bottom. The smaller surfaces are used as optical access ports and electronic feedthroughs, while the top $4\frac{1}{2}$" surface is coupled with a custom-made CF reentrant viewport from Insulator Seal Inc.. The bottom of the chamber is attached to a system of $2\frac{3}{4}$" CF tube which contains a 20liter/s Varian *StarCell* ion pump, an ion pressure gauge, a titanium sublimation filament, and a sealable valve for external pumping.
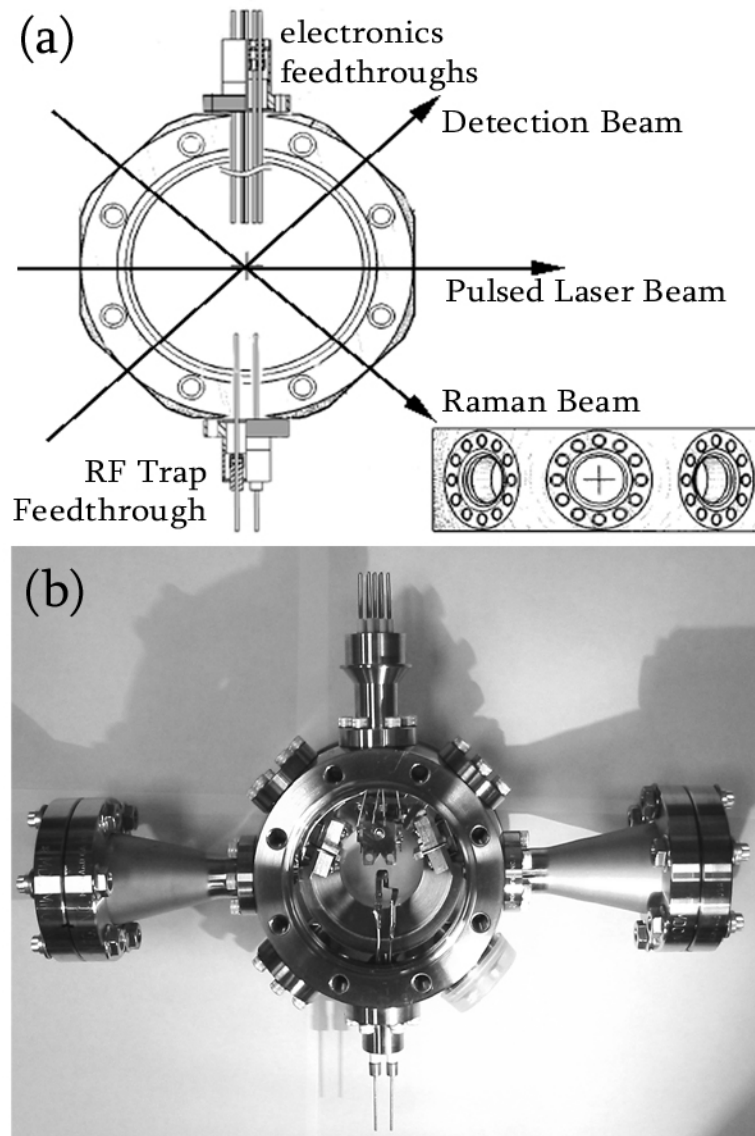
Figure 3.1: (a.) The layout of the spherical octagon used as a trapping chamber. Note that the beams have a 45° geometry, as required, and that the chamber has a narrow ($\sim 1\frac{1}{2}$") side profile (bottom right). (b) The fully assembled trap chamber.
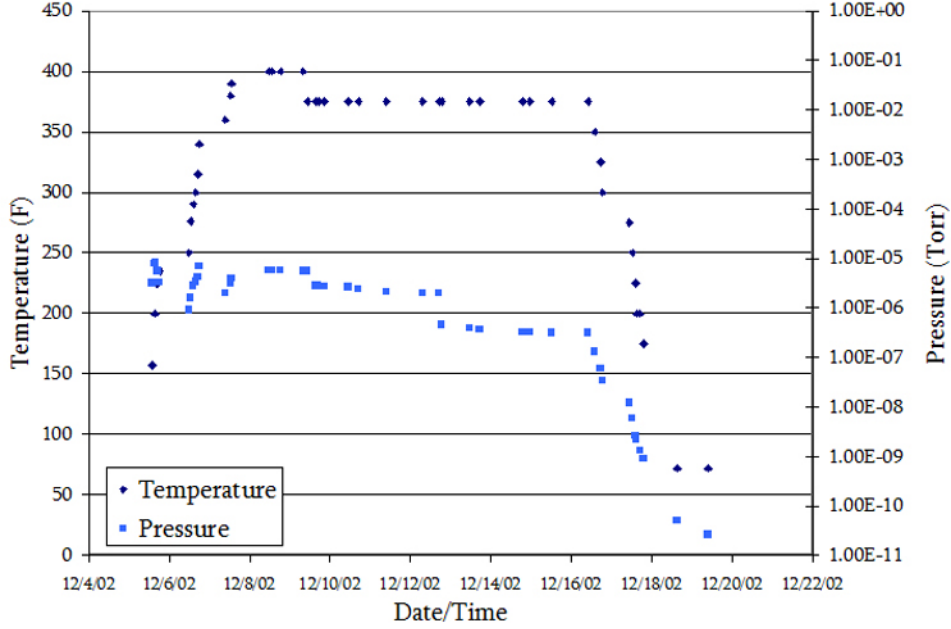
Figure 3.2: This figure shows the pressure in the experimental vacuum chamber (as measured by a Varian ion gauge) and chamber temperature (in °F) as a function of time and date. Note that the chamber went from 3×10^{-6} Torr at room temperature to 2.6×10^{-11} Torr at room temperature after the bake was completed.

Four of the $1\frac{1}{3}$" surfaces are connected to $1\frac{1}{3}$" CF UV-grade fused silica viewports. These are used for transmitting lower power cw beams. Two more of these surfaces are connected to $1\frac{1}{3}$" $\rightarrow 2\frac{3}{4}$" tapered flange adapters. The $2\frac{3}{4}$" surfaces of these adapters are sealed with $2\frac{3}{4}$" CF UV-grade fused silica viewports (see Figure 3.1(b)). These tapered adapters are used for the strong beam so that when the beam enters and leaves the trap it is expanded and significantly less intense. Also, this moves the surface of the viewport farther from the trapping region, lessening the chance that material ablated from the silica might interfere with the local vacuum pressure. Each of these six viewports was AR-coated at 266nm.

The completed chamber was roughed out using a turbopump (to $\sim 1 \times 10^{-6}$ Torr) and subsequently baked to 375°F in a large oven while connected through bellows to an external 200Liter/s ion pump. The motivation for this bake-out was to pump off water
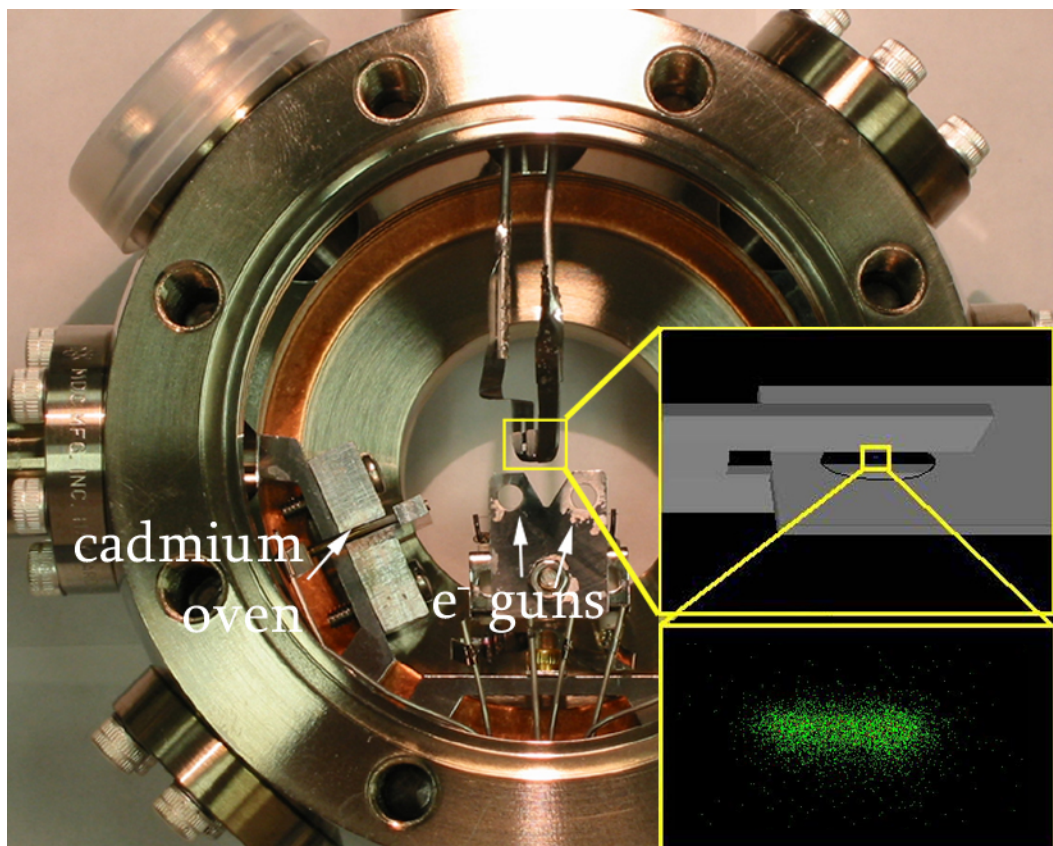
Figure 3.3: A photograph of the in-vacuum electronic instrumentation which is used to trap. Inset are a schematic drawing of the "real" trap electrodes and, further inset, is an image of a horizontally-arrayed crystal of Cd^+ ions trapped within the chamber described herein. This horizontal crystal of ions was observed to undergo rapid phase transitions between horizontal and vertical when a laser cooling beam was applied.

and volatile organics which are nongaseous at room temperature. The bake took place over two weeks as document in Figure 3.2

3.1.2   Trap Electrodes an Associated Electronics

The ion trap built for this experiment has approximately the same design as that described in section 1.1. The electrodes in the ideal case are geometric hyperboloids of revolution, but in this experimental a much simpler design also proves effective. The "ring" and two "endcap" electrodes of an ideal trap are replaced by a "fork" and "ring." The fork electrode used in this chamber is a thin ($\sim$ 5mm wide, 125μm thick)

strip of molybdenum sheet with a 1.3mm-wide notch (in analogy to the endcap spacing in Chapter 1) cut in one end. A 1mm hole (analogous to r_0 in Chapter 1) is drilled near the end of a second thin strip of molybdenum. The trap is constructed by spot welding these two pieces to separate electrical feedthroughs and centering the hole within the notch. Molybdenum is used because of its electrical conductivity and relative rigidity. By holding the notched piece (the fork) at RF ground and placing an oscillating voltage on the piece with the hole (the ring), a trapping potential is produced which is analogous to the hyperbolic case (with some additional multiplicative geometric constant).[1] This configuration is shown inset in Figure 3.3. The dimensions of the fork and ring were selected so that the trap geometric parameter d_0 is a near-integer number – in this case $d_0 \sim 2$.

As mentioned previously, a high RF voltage is applied to the ring electrode with the fork held at RF ground. In order to obtain a large RF voltage which is impedance matched to the trap structure, a helical $\frac{1}{4}$-wave RF resonator was constructed (using the method of MacAlpine and Schildknecht [30]) from plumbing-grade copper pipe and refrigerator tubing. A variable amount of RF produced by an HP 8640B signal generator and amplified by an Isomet RFA-108 +40dB, 8W saturation RF amplifier is coupled inductively into the resonator system. The resonator has an observed resonant frequency of 56.3407MHz and a loaded Q-factor of 295, given by:

$$Q_{\text{res}} = \frac{\nu_+ - \nu_-}{\nu_0},$$

(3.1)

where ν_+ and ν_- are the observed frequencies when the power reflected from the resonator is $\frac{\sqrt{2}}{2}$ times the difference between the observed maximum and minimum reflected power, and ν_0 is the frequency at which the back reflected power is minimized. The resonator is loaded by coupling the end of the resonator helix externally to the vacuum feedthrough which has been spot welded to the ring electrode. The feedthrough spot

---

[1] This is, in general, true for the so-called "Asymmetric Quadrupole" geometry described here. For a more detailed discussion of this trap electrode design see ref [15].
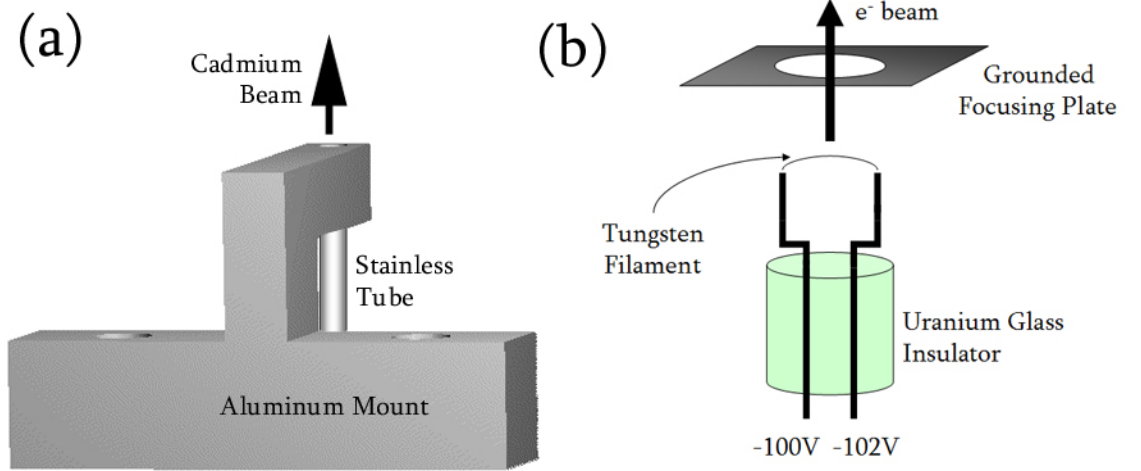
Figure 3.4: Electroncs used to load the RF trap. (a) The neutral cadmium oven. A current applied across the stainless steal tube into which cadmium metal has been placed boils off a directional beam of atoms. The aluminum mounting block acts both as a heatsink for the tube and a means for attaching the oven to the vacuum chamber. (b) The trap electron gun consists of two stainless posts held apart by a uranium glass insulator and connected at one end by a thin tungsten filament. The leads of the gun are biased at $-100V$ and a current is applied across the filament which ejects electrons towards a grounded focusing plate held a few mm away. The electrons are focused through the plate and towards the trapping region. The chamber built for this experiment contains two Cd ovens and two e$^-$-guns.

welded to the fork electrode is connected to a DC voltage supply through a 1kΩ-1μF-1kΩ pi network (which prevents feedback between the RF signal and the floating ground provided by the power supply (this voltage is analogous to U_0, above). The resonator has a breakdown RF insertion power which was unfortunately observed +41dBm. The system presently couples +38dBm of RF power which provides sufficient potential to trap reliably. The trap is loaded by simultaneously directing an atomic beam of neutral cadmium and a beam of medium-energy electrons towards an intersection within the trapping potential. The neutral cadmium beam is produced by passing a current through a thin stainless steel tube which has been crimped closed at one end and placed in a custom-machined aluminum mount with the remaining open end pointing towards the trapping region (see Figure 3.4(a)). Ohmic heating of the stainless boils off a small

amount of neutral, naturally occurring cadmium which was placed into the tube in metal form. We have observed that this atomic beam travels with relatively high directionality away from the end of the tube. Since the tube is held parallel with respect to the optics table, the crimped end is bent slightly downwards to prevent the molten liquid cadmium from flowing out of the tube into the chamber. Two such cadmium ovens were constructed and placed within the vacuum chamber described above using "groove grabbers."

The electron gun used to ionize the neutral cadmium beam within the trapping region is constructed by firmly separating two stainless steel posts with a uranium glass insulator and spot welding a thin tungsten filament across the leads (see Figure 3.4(b)). Passing a current across the leads ejects non-directional electrons from the tungsten filament. By biasing the two leads at $-100V$ and placing a grounded plate with a hole directly above the filament, the electrons are accelerated towards the plate, through the hole, and focused towards the trapping region. An induced current of $\sim 20\mu A$ is observed on the trap electrodes with 129mA of current placed through the leads, confirming that the electron gun is well-aimed. Two such e$^-$-guns are located within the vacuum chamber beneath the trap electrodes (see Figure 3.3). Chapter 4 describes the loading mechanism in further experimental detail.

3.2   The DCR-2 Nd:YAG Pulsed Laser

As was discussed in the previous chapter, the "pushing" laser used in this experiment is the 4th harmonic (266nm) of a QuantaRay DCR-2 pulsed Neodymium Yttrium Aluminum Garnet (Nd:YAG) laser. The DCR-2 is a flashlamp-pumped, two stage, Q-switchable nanosecond pulsed laser outputting an approximate maximum of 800mJ of 1064nm light per pulse when fully Q-switched and amplified. The resonant cavity is of an unstable resonator design with concave back reflector and convex output mirror. The laser operates in three pulse modes – long pulse; Q-switched short pulse; and am-

plified, Q-switched short pulse. The Q-switch mechanism is an electro-optic Pockel's cell which, when "crowbared," dumps the cavity in an approximately 10ns pulse. The optimal pulse repetition rate for the Q-switched cavity (by design) is 10Hz, but this frequency is variable from 1 to 20Hz with less stability in energy per pulse and degraded mode quality as a trade-off. When the Q-switch is off, the laser outputs pulses which are less intense and microseconds long. The Q-switched pulses are optionally amplified in a secondary flashlamp-pumped Nd:YAG cavity.

The process by which the laser produces nanosecond pulses is as follows:

- Step 1: The master oscillator (at 10Hz) produces the oscillator sync trigger pulse (3ms wide, 3.3V high, < 10ns rise/fall time).

- Step 2: This pulse triggers the quarter wave Pockel's cell relay as well as the flashlamp relay.

- Step 3: The Xe flashlamps fire a $\sim 200\mu s$ pulse which optically excites the Nd:YAG crystal in the cavity.

- Step 4: On the trailing edge of the flashlamp pulse, the Pockel's cell voltage is turned off with a 10ns fall time.

- Step 5: $\sim$ 50ns after the Pockel's cell is turned off the laser pulse (lasing the Nd^{3+} $^{4}F_{3/2} \rightarrow^{4}I_{11/2}$ transition) occurs with an 8 to 9ns envelope width.

- Step 6: The Pockel's cell voltage is ramped back to maximum over $\sim 20\mu s$ and then dropped back to zero roughly 1ms later, ending the pulse sequence.

The spatial and temporal modes of this pulse appear non-Gaussian, even in the far-field limit (as discussed previously). The (non-Gaussian) diameter of the beam is on the order of 7mm. For a discussion of the output spatial modes of an unstable resonator cavity, see ref. [31]. The direct output from the laser is linearly polarized and oriented vertically

for maximal second harmonic generation (SHG). At the fundamental, the stability in energy per pulse is $\pm 1\%$, but this figure degrades through subsequent optical frequency doubling.

The Nd:YAG fundamental produced by the DCR-2 is passed directly through an angle-tuned, temperature-regulated deuterated potassium dihydrogen phosphate (KD*P) crystal where it undergoes type II SHG. A portion of the fundamental is converted to 532nm light (approximately 50%) while the remaining portion is transmitted. The conversion efficiency can be adjusted linearly by rotating the polarization of the fundamental. The second harmonic pulses are shorted from 8-9ns to 6-7ns and have a pulse-to-pulse energy stability of $\pm 3\%$. The co-propagating second harmonic and fundamental beams are made incident upon a 1064nm/532nm dichroic mirror from which the second harmonic is reflected, and the fundamental is transmitted and eliminated in a high-power beam dump.

The reflected second harmonic is passed through a second KD*P crystal cut for fourth harmonic generation (4HG). This crystal is angle-tuned, but does not need to be
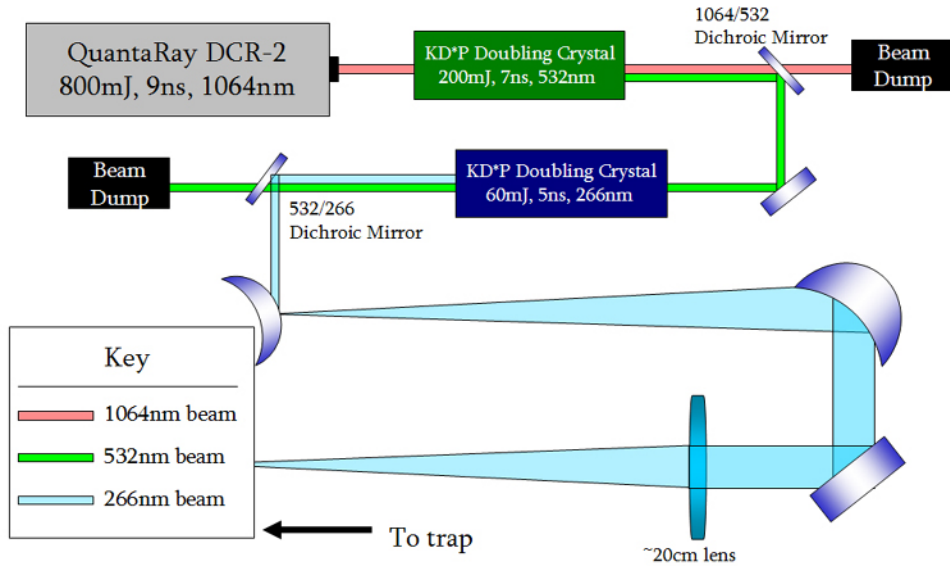

Figure 3.5: Process diagram for 266nm pushing beam generation.

temperature regulated. Conversion efficiency from 532nm to 266nm is on the order of 40%. The resulting fourth harmonic pulses are vertically polarized and 4-5ns in length with an energy stability of $\pm 4\%$. The remaining second harmonic is filtered out by two 532nm/266nm dichroic mirrors and a sequence of 266nm HR coated steering mirrors.

3.3   Visualizing and Measuring the Ion

3.3.1   The Detection Beam

The position and state of the ion are determined by resonantly scattering ~ 1ms pulses of 214.5nm σ^+-polarized light from the $S_{1/2} \left| 1, 1 \right\rangle \leftrightarrow P_{3/2} \left| 2, 2 \right\rangle$ cycling transition. This light is generated through the process shown in Figure 3.6. A ~ 3W Coherent Verdi V10 (DPSS Nd:YAG$\times 2$, 532nm) laser pumps a continuous wave (cw) Coherent MBR 110 Titanium Sapphire laser cavity. By tuning the etalon and servo of this cavity, the wavelength of the Ti:Sapphire is set to ~ 858.0300nm and is is tunable and mode-hop-free over a few GHz. This beam is coupled into a SpectraPhysics Wavetrain lithium borate (LBO) optical frequency doubling cavity tuned for converting 858nm$\rightarrow$ 429nm. The ~ 400mW of 429nm light produced in this cavity is then sent into a similar Wavetrain barium borate (BBO) frequency doubling cavity (tuned for 429nm$\rightarrow$ 214.5nm generation). The end result is ~ 10mW of tunable 214.5nm UV light light (the desired detection beam).

In the near future, the first three components of this system (the Verdi V10, MBR 110, and LBO WaveTrain doubler) will be replaced by a Toptica TA-SHG 100 which consists of a tunable external cavity diode laser of Littrow design at 858nm injected into a tapered amplifier and doubled in a potassium niobate optical frequency doubling cavity.

The wavelength of the detection beam is made stable to within 1MHz through use of a Doppler-free spectroscopic Te_2 optical frequency reference cell. Doppler-free

spectroscopy is a well-established method for stabilizing tunable cavity lasers [32]. The Te$_2$ molecule has a rich spectrum of transitions in the visible, including a line near the 858.0300nm second harmonic at 429.0150nm. This line (referenced as #989 in the Te$_2$ spectral atlas [33]) lies at 429.0140nm.

In order to observe this line, a small fraction of the 429nm beam is picked off using a beamsplitter and subsequently separated into "pump" and "probe" beams for nonlinear spectroscopy. The "pump" beam carries 5 times more power than the "probe" and is transmitted through a Te$_2$ gas cell (at $\sim 500^o$C in an oven) along an arbitrary $+k$-vector. This beam interacts with those Te$_2$ molecules moving at sufficient velocity $+v$ so that the current wavelength of the laser is Doppler shifted onto resonance with the desired transition. Having absorbed the incident photons, these molecules are said to be "saturated" or unable to absorb any further light; they have removed some number
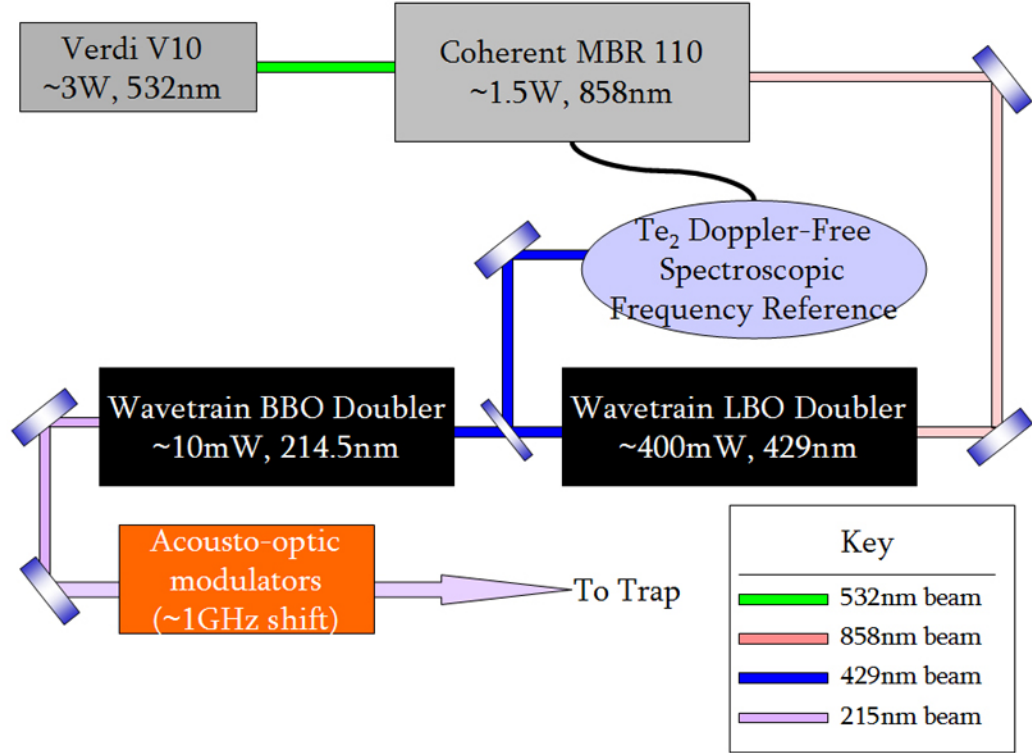

Figure 3.6: Process diagram for detection beam generation.

of photons from the incident beam. By scanning the wavelength of the laser and simply observing the absorption of the "pump" beam, the profile of the transition takes the shape of the molecular distribution of speeds – a broad Gaussian on the order of a few hundred megahertz wide.

In order to obtain resolution of the line below so-called Doppler broadening, a second, less intense "probe" beam is directed through the cell along the $-k$-vector. These photons interact with molecules having velocity $-v$ (on the other wing of the Gaussian), again saturating this small population. With both beams incident simultaneously, the two saturated populations on either wing of the Gaussian are called "Bennet holes." (See Figure 3.7.) The shape of these Bennet holes is approximately the Lorentzian shape of the natural line.

The two Bennet holes do not interact with one another - they are separate populations of molecules - until the wavelength of the laser is such that those shifted onto resonance with the "pump" beam are also shifted onto the "probe" beam. As the laser is scanned exactly onto resonance with the line, the more intense "pump" beam saturates the cell and the transmission of the "probe" beam increases while the two Bennet
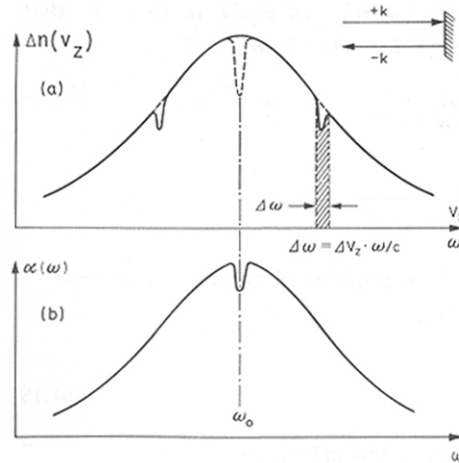

Figure 3.7: The convergence of Bennet holes "burned" into the Gaussian lineshape of a gas yields a Lamb dip which bears the shape of the natural molecular transition. Figure taken from [32].

holes overlap (since the population resonant with the "probe" beam has already been saturated). This sudden transmission increase of the "probe" is called a "Lamb dip" and takes approximately the shape of the natural line. By measuring the transmission of both beams (the pure Gaussian "pump" transmission and the Gaussian with Lamb dip transmission of the "probe") with a New Focus Nirvana-brand photodetector, and then subtracting the electronic signals, the Gaussian is subtracted away and what remains is an electrical signal in the ~ 15MHz-wide shape of the desired transition.

This signal is differentiated electronically by the Nirvana and fed into the circuit depicted in Figure 3.8(a) where is integrated and returned to the external servo scan of the Ti:Sapph fundamental, increasing or decreasing the wavelength so that the laser is always centered on the Lamb dip to within a few percent of the width of the dip (or a few kHz). The circuit of Figure 3.8(b) is an external, manual wavelength scanning device (essentially a linear voltage supply) used to find and measure the desired line. With the laser locked to the desired Te_2 line, its frequency is stable and precisely known within the measured accuracy of the line.

The Te_2 feature to which the laser is locked is not on resonance with the Cd^{111} cycling transition at 858.0261nm ($\sim$ 1GHz in the IR from the lock), so a small bit of additional frequency adjustment is necessary. With the laser locked, the beam is coupled through acousto-optic modulators (AOMs) driven by Hewlett Packard 8640B signal generators. These AOMs, down-beam from the Doppler-free beamsplitter, modulate the frequency of the beam, compensating for the distance between the tellurium feature and the cadmium feature. Since 8640B generators are frequency stable to well under a kilohertz, the stability of the lock remains intact.

3.3.2 Imaging and Measurement Apparatus

Trapped ions are imaged by collecting laser light scattered from the ion in some manner of position-resolving photodetector (MCA photomultiplier tube, CCD camera,
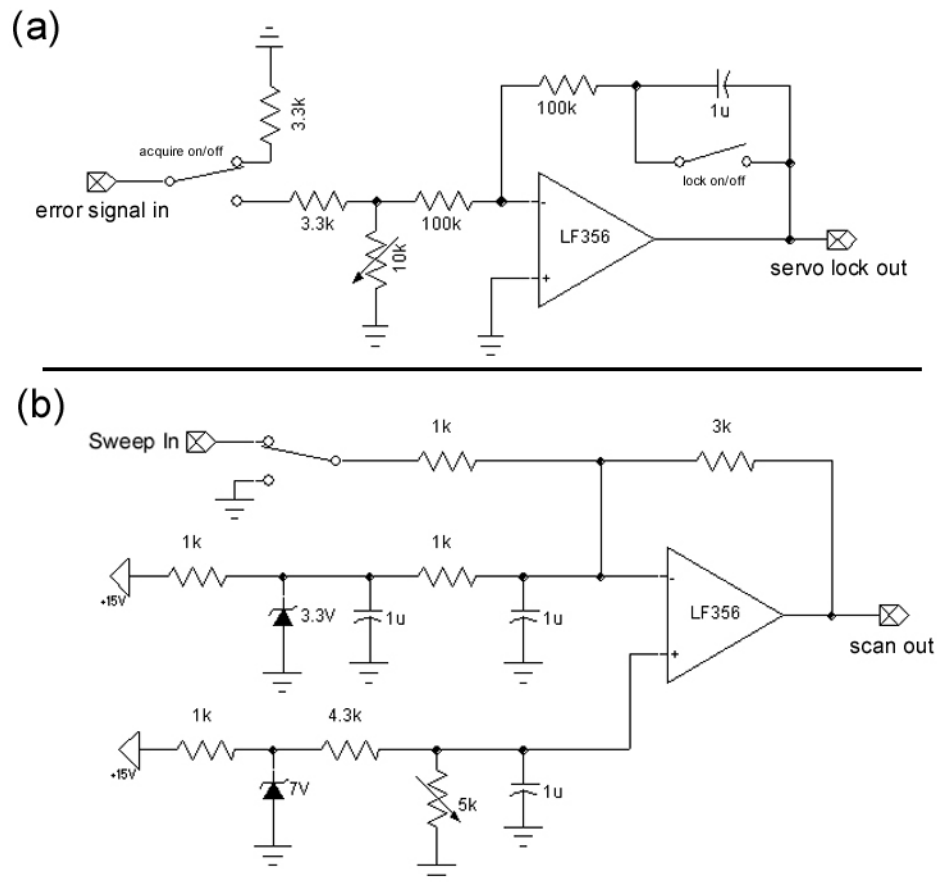
Figure 3.8: Te$_2$ optical frequency reference servo lock circuit diagrams. (a) The Lamb dip observed electronically through saturated absorption spectroscopy, corresponding to the non-Doppler broadened 23309.2481cm^{-1} molecular transition in Te$_2$, is either disregarded, differentiated and used as a weak "aquire" signal to reference a Ti:Sapph cavity, or integrated and used as a strong "lock" signal to reference the cavity. The gain of the servo is adjusted through a 10kΩ potentiometer. b.) A simple DC voltage source with a switchable sweep signal used to tune the Ti:Sapph cavity linearly, scanning the laser's wavelength in order to located the desired Te$_2$ feature.

etc.). For this experiment, a position-sensitive, UV-active photomultiplier tube apparatus built by Quantar Technology, Inc. was employed with a more efficient Hamamatsu PMT used for data collection. Light scattered from ions in the trap is collected by a CVI triplet lens with a focal length of 21cm at a distance of 7mm above the ion trap (made possible using the $4\frac{1}{2}$" re-entrant window discussed above). This image is spatially filtered for background light using a 50μm pinhole inside of a 1" diameter camera tube which runs the length of the imaging apparatus (see Figure **??**). This section of camera tube is position on a Line Tool X-Y-Z translation stage which allows imaging over the entire spatial extent of the trapping region. The light from the triplet next enters a columnating doublet lens and is sent through a 0°-incidence 266nm HR-coated suprasil optical blank which filters 99.9% of 4$^{\text{th}}$-harmonic YAG light and transmits $\sim 30\%$ of the detection light. This optic is in place to prevent damage to the high sensitive PMT imaging devices at the end of the imaging apparatus from the high-intensity pushing beam light.

Finally the image enters a custom-built, black-anodized light-tight aluminum box mounted $5\frac{1}{2}$' above the optics table. Contained within the box is a *Hamamatsu* UV-sensitive PMT ($\sim 50\%$ quantum efficiency and not position-resolving) and the aperture of a UV-sensitive Quantar microchannel plate PMT camera ($\sim 1\%$ quantum efficiency). The image can be switched between the two devices using a 214.5nm HR-coated mirror on a remote-controlled automated flip mount. Images taken using the Quantar can be seen in chapter 4. A single ion, brightly fluorescing in the trap produces ~ 8K counts per second while the Hamamatsu PMT yields ~ 85K counts per second. In general then the Quantar will be used to resolve and characterize ions in the trap while the Hamamatsu will be used for data collection, as described in the previous chapter.
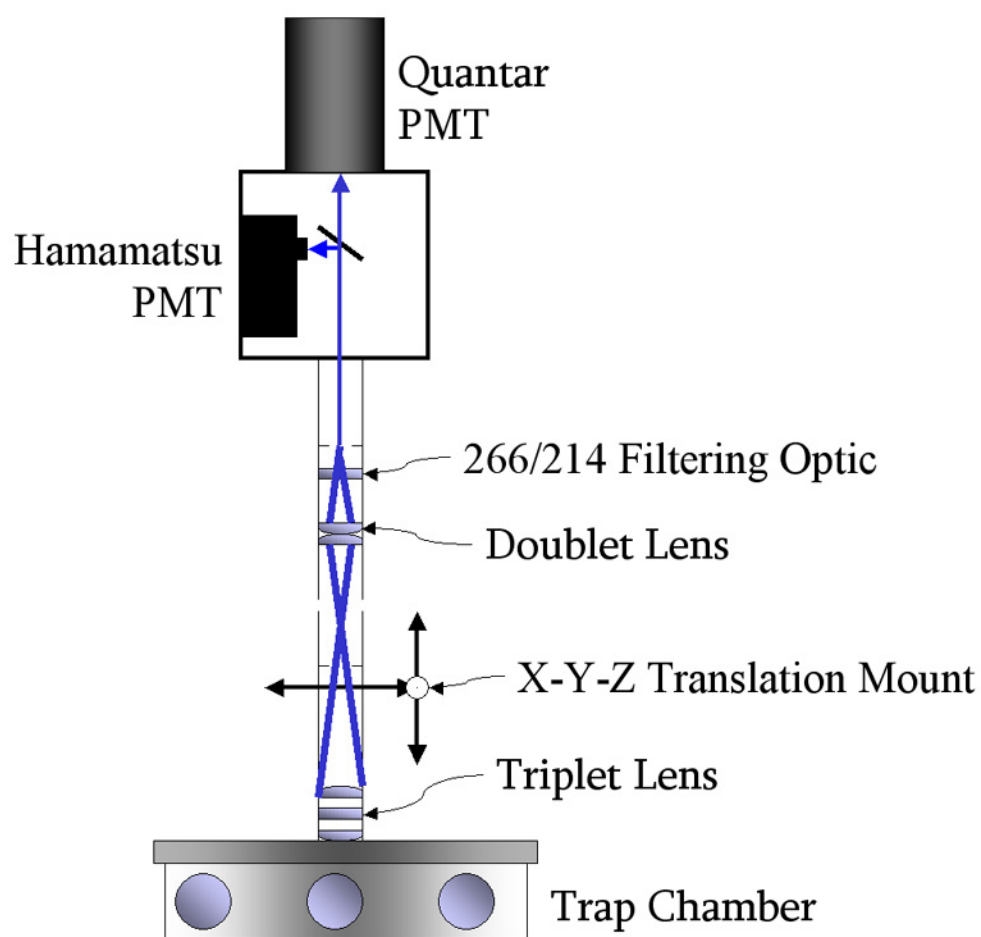
Figure 3.9: Imaging apparatus for detecting trapped Cd^+ ions.

Chapter 4

Data and Analysis

4.1   Observed Trap Characteristics

As of the writing of this thesis the trap described in the previous chapter has successfully and reliably been used to trap and image Cd^+ ions. The probability of successfully loading an ion (of any isotope) during a single firing of both e^--guns and Cd ovens is a function of the current passed through each and can be varied from 100% at large currents to as little as 5% or less at lower currents. Loading during every trial is undesirable as this indicates an over-saturation of the trapping region with neutral cadmium. Such an over-saturation has been observed in other experiments in this laboratory to coat vacuum viewports (limiting laser transmission) and in-vacuum electronics (producing potential electrical shorts). Another problem that can potentially result is degraded local vacuum in the trapping chamber which would, in turn, increase the cross section for a collision of trapped ions with background gas that might subsequently eject the ions from the trap.

A reliable scheme for loading successfully during approximately 10% of attempts has been found to consist of passing $\sim 1.2A$ through the first of two e^--gun filaments and $\sim 1.3A$ through the first of two Cd ovens for a period of around 70s with the detection laser set to 214.5075nm. This results in an increase in pressure at a non-local ion pressure gauge of about one order of magnitude (or from $\sim 2 \times 10^{-11}$ Torr to $\sim 2 \times 10^{-10}$ Torr). In order to maintain the local vacuum, a period of 10 minutes

is allowed between subsequent attempts to load during which the vacuum pressure generally returns to its original value. The laser wavelength is crucial because it puts the beam to the red of the resonant frequency for all isotopes of cadmium thus preventing "Doppler heating" and ejection of the ions as soon as they are loaded. Ions are imaged by centering and focusing the detection beam through the trapping region, locating each of the two "sides" of the trap (inside edges of the ring electrode which lie parallel to one another) using the micrometer-mounted CVI triplet lens described previously and using these as guides to the center of the trapping region (towards the local RF zero, or the place at which ions are expected to experience strongest confinement).

The laser wavelength is scanned from 214.5074nm (resonant for ^{116}Cd$^+$) to 214.5065nm (resonant for ^{111}Cd$^+$). As the resonant frequency for a given isotope is approached, ions of this isotope in the trap begin to fluoresce and are resolved using the imaging apparatus discussed previously. Integrated images of this fluorescence have been captured and are shown in Figure 4.1. We have observed that in this particular trap that multiple ions tend to load simultaneously, producing a cloud-like image which often fluoresces at a number of frequencies (corresponding to the different isotopes which comprise the cloud). It also been observed that by removing and re-introducing the detection beam that these clouds will momentarily crystalize into a vertical or horizontal crystal such as that shown in 4.1(d). Single ions (4.1(c)) have also been observed with trapping times in excess of 3 hours.

It has been found that ions stored in the trap with the fork electrode held at ground ($U_0 = 0$) are poorly resolved even as single ions. The cause of this phenomenon was determined to be secular motion driven by spurious electric fields resulting from asymmetries in the trap and charge buildups on adjacent objects. The effect can be counteracted by applying a static **negative** voltage to the fork (tightening the trap along the vertical axis). It was found that an applied voltage between $U_0 = -14$V and $U_0 = -20$V provides much better spatial resolution. Voltages more negative than
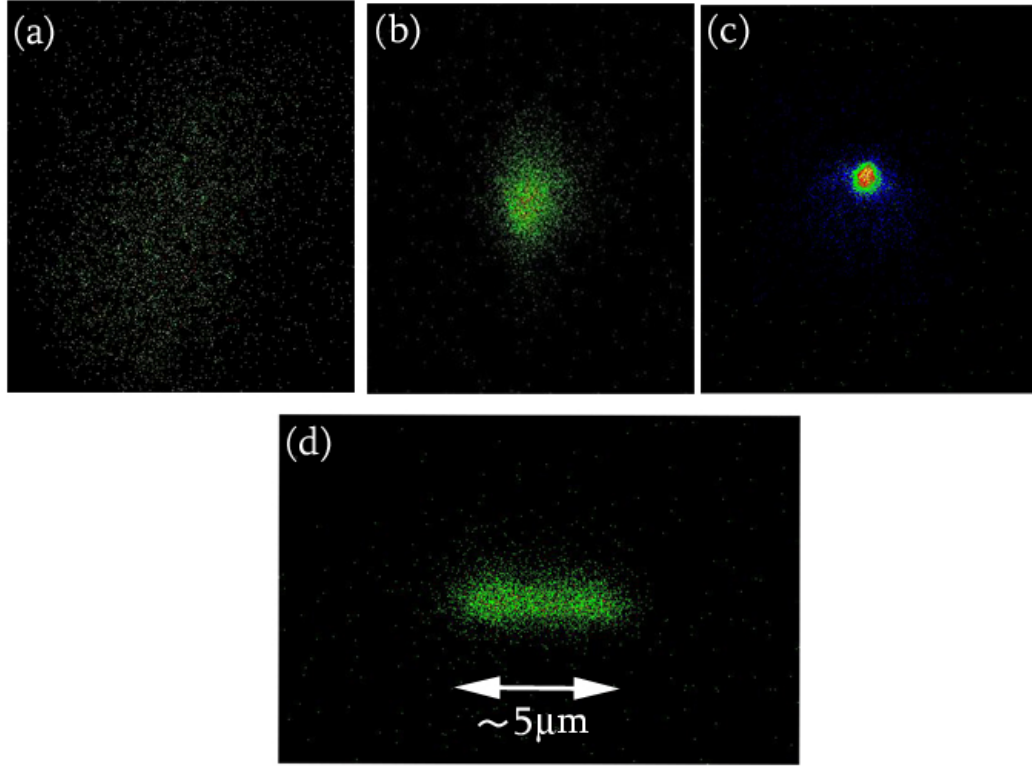
Figure 4.1: A collection of images of ions confined in the Paul trap built for this experiment. (a) A diffuse cloud of trapped ions fluorescing weakly at 214.5074nm (the first ions seen in this trap). (b) A more clearly resolved cloud of ions again fluorescing at 214.5074nm. (c) A single, well resolved ^{114}Cd$^+$ ion stored in the trap with a bias voltage $U_0 = -14$V applied to the fork electrode. (d) A 5μm-long, horizontally arried crystal of trapped ions (the number of ions in the crystal is either three or four, though the precise number was not resolved).

$U_0 = -20$V result in ejection of the ion (which can be thought of the trap becoming "too tight" in the vertical direction and forcing the ion out). Positive fork electrode voltages, as expected, tend to weaken the trap resulting in poor spatial resolution of the ion and, at around +15V, ejection of the ion.

4.2   Data and Observations

At present the pushing laser as been successfully coupled through the trap with no observable damage to the vacuum instrumentation and collection of data from the Ramsey experiment discussed in the previous chapter is expected to begin within the next two weeks (i.e.: mid-April, 2003).

4.3   Future Directions

While initial experimental data is presently pending, there a variety of future considerations which might bring the Cirac-Zoller pushing gate further towards fruition. First is the implementation of a more suitably engineered pushing laser. The Positive Light Indigo DUV tunable, pulsed Ti:Sapphire laser discussed in chapter 2 (or the similar Quantronix Proteus tunable Ti:Sapphire) would be particularly well suited to the task as it offers a much larger repetition rate with precisely the wavelength (222.76nm) necessary for the interactions of the laser with the $|0\rangle$ state to exactly cancel. This laser offers a kilohertz repetition rate which, in the long term, might be too slow to practically implement logic operations. In the future it might be beneficial to explore picosecond pulsed Ti:Sapphire lasers with larger repetition rates and perhaps even bring the experiment into the possible regime of real-time quantum feedback.

Another future concern is the implementation of the array of "microtraps" described by Cirac and Zoller [2]. Current work within this research group by M. Madsen, D. Stick and W. Hensinger is yielding potentially useful grids of microscopic traps with characteristic dimensions on the order of 20μm. This work, currently in progress and

the subject of an upcoming research paper, is further discussed in Appendix B.

4.4   Conclusions

We have described the design and initial operation of instrumentation for the purpose of measuring strong laser field-induced spin-dependent a.c. Stark shifts in Cd^+ ions. We have thoroughly discussed the theory underlying spin-dependent dipole forces in hydrogen-like systems such as Cd^+. The apparatus built and installed exclusively for this experiment includes a high-power nanosecond pulsed laser, a ultrahigh vacuum trapping chamber, electronics requisite to produce a working ion trap, a deep UV (214.5nm) detection laser, and a system for detecting light scattered from ions within the trap. This apparatus is pictured in Figure 4.2 as it is currently installed on our optics bench. We expect to begin taking data within the next three weeks and this final chapter will be revised with results from the first run.
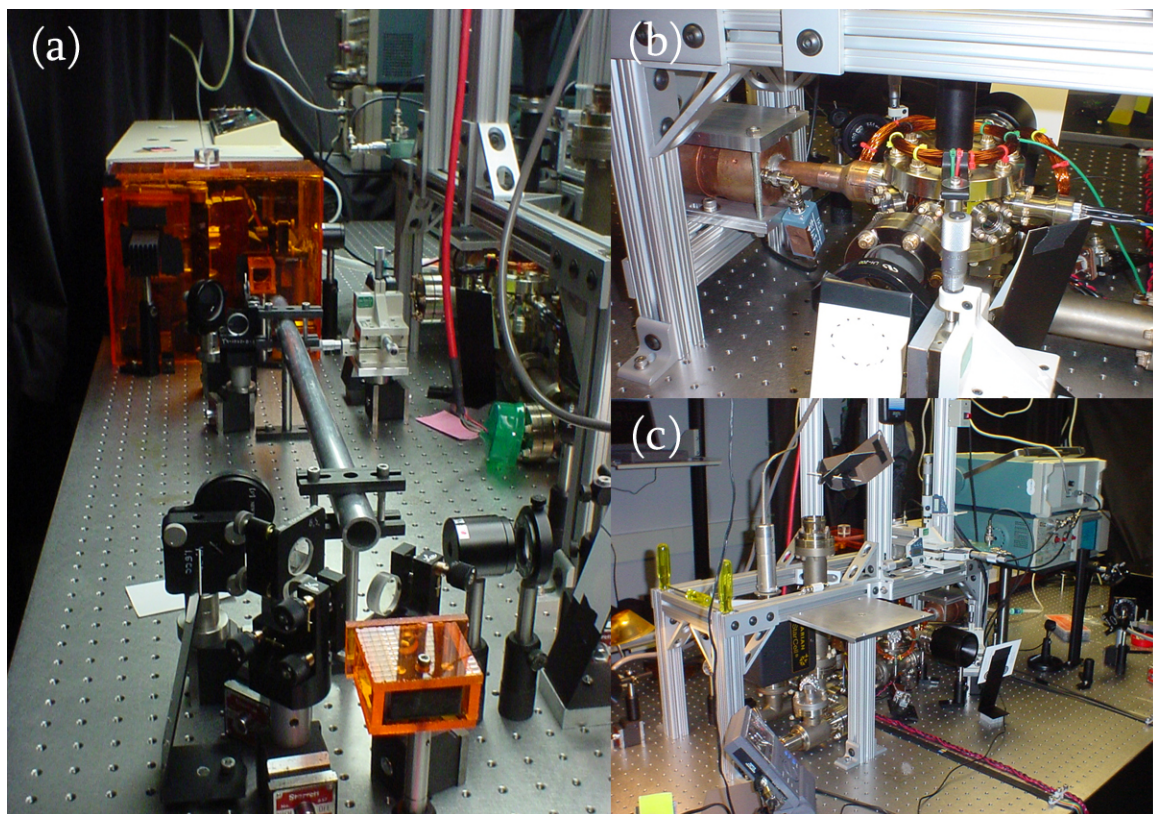
Figure 4.2: The experimental apparatus contructed for this experiment. (a) The DCR-2 pulsed laser with its associated doubling, quadrupling, filtering and focusing optics. (b) The trapping chamber as it currently sits on the table. (c) A side view of the trapping chamber and the lower half of the 80/20 extruded aluminum table which holds the imagining apparatus above the ion trap.
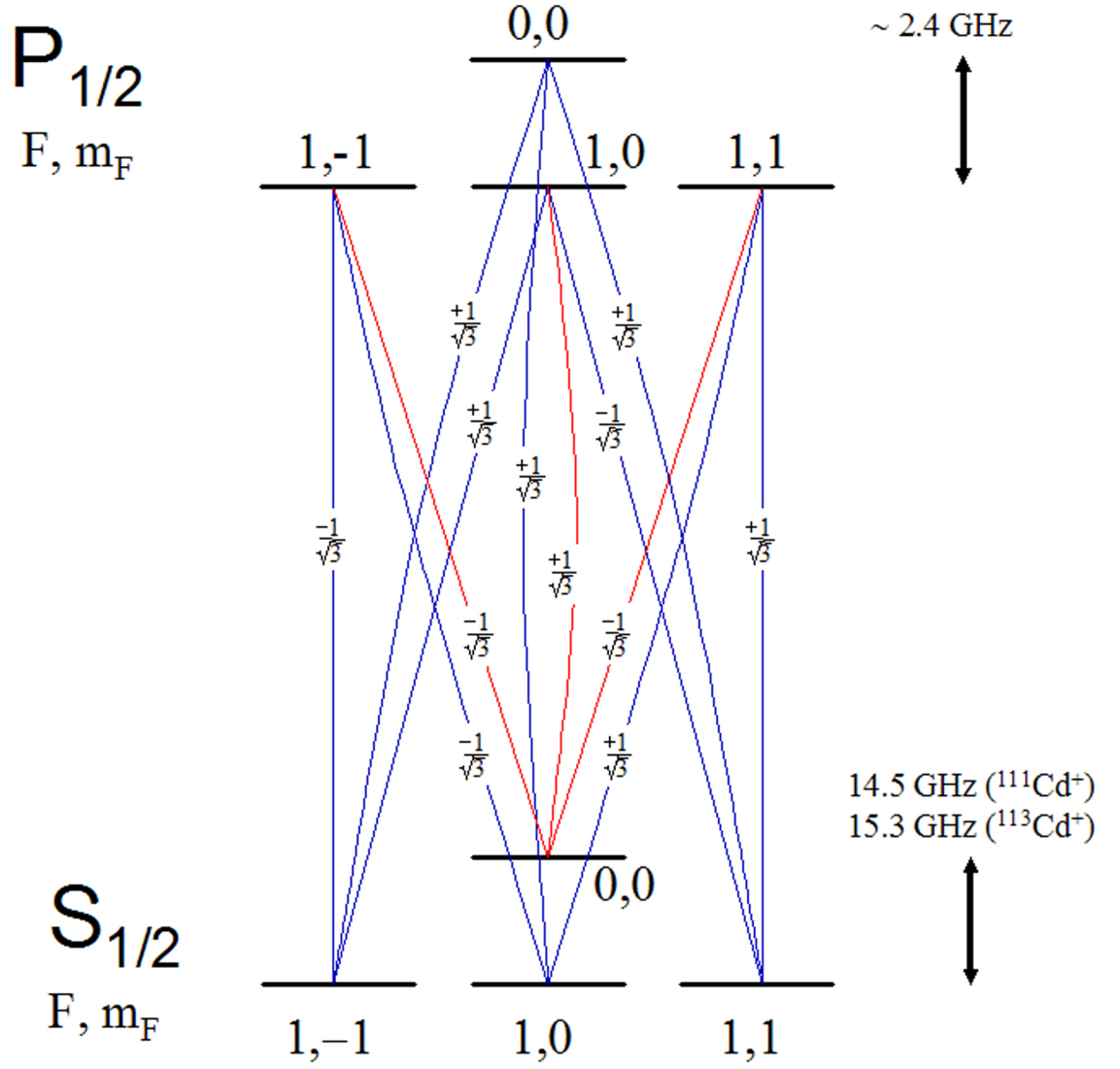
Appendix   A

Matrix Elements

P$_{1/2}$

F, m$_F$

0,0

1,-1   1,0   1,1

~ 2.4 GHz

$\frac{+1}{\sqrt{3}}$ $\frac{+1}{\sqrt{3}}$

$\frac{+1}{\sqrt{3}}$ $\frac{-1}{\sqrt{3}}$

$\frac{+1}{\sqrt{3}}$

$\frac{-1}{\sqrt{3}}$ $\frac{+1}{\sqrt{3}}$ $\frac{+1}{\sqrt{3}}$

$\frac{-1}{\sqrt{3}}$ $\frac{-1}{\sqrt{3}}$

$\frac{-1}{\sqrt{3}}$ $\frac{+1}{\sqrt{3}}$

14.5 GHz (^{111}Cd$^+$)
15.3 GHz (^{113}Cd$^+$)

0,0

S$_{1/2}$

F, m$_F$

1,−1   1,0   1,1

Figure A.1: Relative transition amplitudes for transitions between hyperfine levels (in the $|F, m_F\rangle$ basis) for the Cd$^+$ D1 (S$_{1/2} \leftrightarrow$P$_{1/2}$) line at 226.5nm [34].
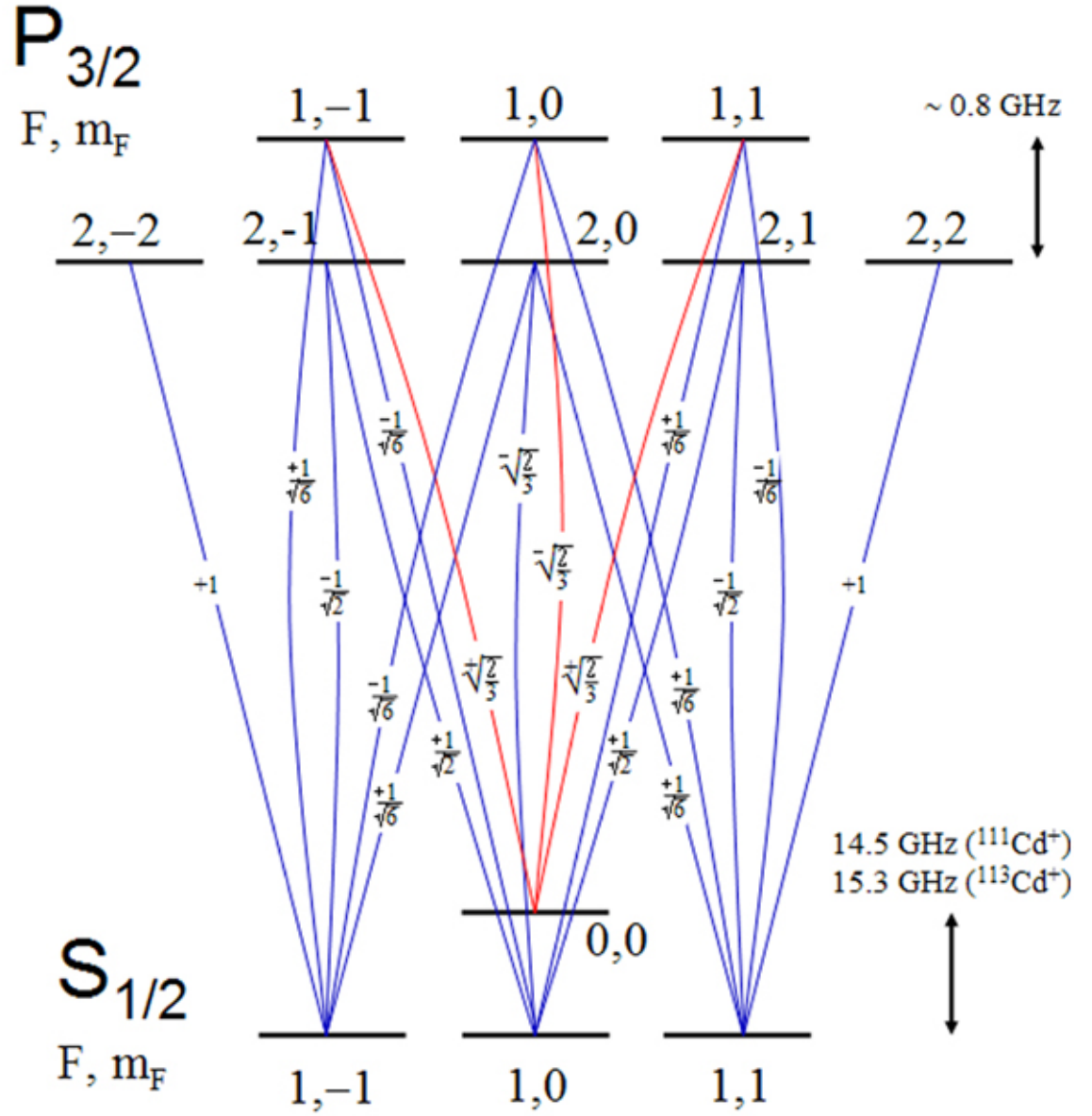
Figure A.2: Relative transition amplitudes for transitions between hyperfine levels (in the $|F, m_F\rangle$ basis) for the Cd^+ D2 ($\mathrm{S}_{1/2} \leftrightarrow \mathrm{P}_{3/2}$) line at 214.5nm [34].

Bibliography

[1] B. Blinov et al., Phys. Rev. A **65**, 040304(R) (2002).

[2] J. I. Cirac and P. Zoller, Nature **404**, 579 (2000).

[3] P. K. Ghosh, Ion Traps (Claredon Press, Oxford, 1995).

[4] D. J. Wineland, R. Drullinger, and F. Walls, Phys. Rev. Lett. **40**, 1639 (1978).

[5] W. Neuhauser, M. Hohenstatt, P. Toschek, and H. Dehmelt, Phys. Rev. Lett. **41**, 233 (1978).

[6] R.S. Van Dyck Jr., P.B. Pschwinberg, and H.G. Dehmelt, Phys. Rev. Lett. **59**, 26 (1987).

[7] S. Diddams et al., Science **293**, 825 (2001).

[8] J. I. Cirac and P. Zoller, Phys. Rev. Lett. **74**, 4091 (1995).

[9] C. Monroe, D. M. Meekhof, B. E. King, W. M. Itano, and D. J. Wineland, Phys. Rev. Lett. **75**, 4714 (1995).

[10] D. Kielpinski, C.R. Monroe, and D.J. Wineland, Nature **417**, 709 (2002).

[11] A. Sørensen and K. Mølmer, Phys. Rev. Lett. **82**, 1971 (1999).

[12] S. Gulde et al., Nature **421**, 48 (2003).

[13] T. Calarco, J. Cirac, and P. Zoller, Phys. Rev. A **63**, 062304 (2001).

[14] M. Sasura and A. Steane, quant-ph/0212005, 2002.

[15] B. E. King, Quantum State Engineering and Information Processing with Trapped Ions, PhD thesis, Department of Physics, University of Colorado, 1999.

[16] D. J. Wineland et al., Journal of Research of the National Institute of Standards and Technology **103**, 259 (1998).

[17] C. Cohen-Tannoudji, B. Diu, and F. Laloë, Quantum Mechanics (John Wiley & Sons, New York, 1977).

[18] E. Merzbacher, Quantum Mechanics (John Wiley & Sons, New York, 1998).

[19] D. Lide, editor, <u>Handbook of Chemistry and Physics</u> (CRC Press, Boca Raton, 2001).

[20] P. Lee <u>et al.</u>, Submitted, 2002.

[21] D. Suter, <u>The Physics of Laser-Atom Interactions</u> (Cambridge University Press, Cambridge, 1997).

[22] P. Meystre, <u>Atom Optics</u> (Springer, New York, 2001).

[23] H.J. Metcalf and P. van der Straten, <u>Laser Cooling and Trapping</u> (Springer, Stony Brook, NY, 1999).

[24] S.L Rolston, C.R. Monroe, Ed., and F. De Martini, Ed., <u>Proceedings of the International School of Physics "Enrico Fermi" - Experimental Quantum Computation and Information</u> (IOS Press, Amsterdam, 2002).

[25] M. Nielsen and I. Chuang, <u>Quantum Computation and Quantum Information</u> (Cambridge University Press, Cambridge, 2000).

[26] B. Blinov, C. Monroe, D. Moehring, and R. Miller, pending (2003).

[27] H. Häfner <u>et al.</u>, PRL (accepted) (2003).

[28] J. Poyatos, J. Cirac, R. Blatt, and P. Zoller, Phys. Rev. A **54**, 1532 (1995).

[29] P. Bucksbaum, private communication, 2003.

[30] W. MacAlpine and R. Schildknecht, Proceedings of the IRE **Dec.**, 2099 (1959).

[31] A. Siegman, <u>Lasers</u> (University Science Books, Mill Valley, CA, 1976).

[32] W. Demtröder, <u>Laser Spectroscopy</u> (Springer-Verlag, New York, 1981).

[33] J. Cariou and P. Luc, <u>Atlas du Spectre D'Absorption de la Molecule de Tellure</u> (Laboratoire Aime - Cotton CNRS II, Orsay, France, 1980).

[34] C. Monroe, private communication, 2003.